JRC Scientific and Technical Reports

Development of the Mandrel Test for Controlled Displacement of Zircaloy tubes

Summary of Initial Work 2007

K-F Nilsson, C. Chenel-Ramos, V. Vokál, J. Mendes and O. Martin

EUR 23283 EN - 2008

JRC EUROPEAN COMMISSION

ie Institute for Energy

EUR 23283 EN - 2008

The Institute for Energy provides scientific and technical support for the conception, development, implementation and monitoring of community policies related to energy. Special emphasis is given to the security of energy supply and to sustainable and safe energy production.

European Commission
Joint Research Centre
Institute for Energy (IE)

Contact information

Address: P.O. Box 2, 1755ZG Petten, The Netherlands
E-mail: karl-fredrik.nilsson@jrc.nl
Tel.: +31 224 565420
Fax: +31 224 565641

http://ie.jrc.ec.europa.eu/
http://www.jrc.ec.europa.eu/

JRC43877

EUR 23283 EN
ISSN 1018-5593

Luxembourg: Office for Official Publications of the European Communities

Printed in Luxembourg

Abstract

This report describes some initial work at IE to develop a displacement controlled test for testing the material properties of spent fuel cladding tubes. The objective is to have a test which allows stable failure under increasing and for which the level of axisymmtery can be controlled. The cone-Mandrel test consists of a set of arc-shaped segments placed inside a section of a Zircaloy tube and pushed outwards by the vertical displacement of a conical shaft. The cone-mandrel is first developed for un-irradiated conditions but the test should also be applicable for irradiated components in hot cells at ITU. The report describes the practical implementation of the cone-mandrel with 8 segments and applied to three specimens. The tests show that the cone-mandrel can be used to attain controlled displacements until failure. The load is not accurately monitored for very low loads due to misalignment between cone, segments and tube. It is, however, straight-forward to compensate for this effect from the registered displacement/strain curve. The tested specimens were subsequently analysed by fractographic studies. The main fracture was by shearing along lines that make 45° angle with the axial and circumferential directions. The tests were simulated by non-linear finite element (FE) calculations. The finite element calculations simulated the experimental observations quite well. The FE calculations also allowed us to better understand the failure by necking and the deviation of axi-symmetric loading due to stress concentrations at the end of the segments. Furthermore the cone is also subjected to plastic deformation. The plastic deformation of the cone and the deviation from axi-symmetric load conditions can be reduced by increasing the number of segments. To this end mandrels with 6, 8 and 10 segments were analysed. The conclusion is that one should use at least 8 segments and that one should use a harder material for the cone.

Introduction

For spent fuel storage the cladding that surrounds the fuel pellets can be seen as the first barrier against release of radionuclides. The integrity of the cladding is very important for long-term storage and transport since spent fuel needs to be handled before it goes into final disposal or being processed. During reactor operation the zircaloy will corrode ($2H_2O + Zr \rightarrow ZrO_2 + 4H$) whereby hydrogen is released and an oxidation layer is formed. The oxidized material has a larger volume than the base metal. This volume difference leads to a residual stress field in the cladding with compressive stresses in the oxidized part and tensile stresses in the base metal. The hydrogen diffuses into the base material but precipitates as hydrides ($4H + 2Zr \rightarrow 2ZrH_2$) in the circumferential direction when the temperature drops. The hydrides have a tendency to re-orient as radial hydrides during drying of the fuel, which leads to embrittlement of the cladding as shown in Figure 1. Cracks may initiate from such hydrides and then propagate to become a through-wall crack. The residual stresses may also play an important role in the crack propagation. The radial hydrides may reduce the cladding's ductility by more than one order of magnitude. Global failure of the fuel cladding may ensue when an axial crack propagates in a splitting mode. This is one of the most important failure mechanisms for the cladding.

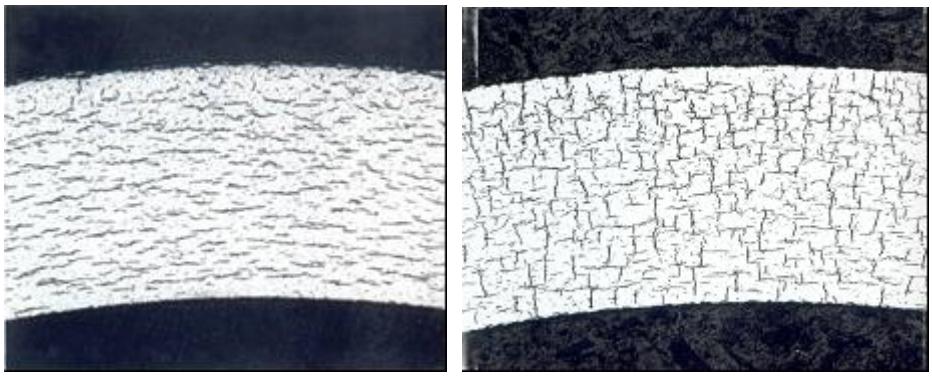

a) b)

Figure 1 Zircaloy cladding tube with a) circumferential and b) radial hydrides

To better understand the failure of zircaloy claddings a combination of mechanical models at the appropriate scale, microstructural analysis and mechanical component testing need to be carried out. The mechanical component test should be representative for the loads that may occur and the resulting loading should be as simple as possible to analyse. A third requirement for mechanical testing is that failure should be as stable as possible in the sense that failure would occur progressively under increasing load. Load controlled tests, such as the pressure test, is often used for cladding tubes. It fulfils the first two requirements but failure would normally be unstable. This is the reason why this test is often referred to as a "burst test". The Mandrel test is a displacement controlled test for which the failure is expected to be much more stable.

Figure 2 illustrates the basic concept of the Mandrel test. A cone is displaced into a set of segments that exert a controlled displacement on the cladding tube. The test is a good representation of the swelling of the fuel pellets. The segments, however, are discrete entities and complex stress concentrations will occur in the cladding at edges of the segments. The segments could be a way to model cracked fuel but a drawback is that the loading becomes more complex to analyze. With increasing number of segments the stress concentrations will become smaller and the load will be more axisymmetric. This would render the test more suitable for material characterization tests such as fracture toughness and for the investigation of basic failure mechanisms.

The cone-Mandrel test is part of a collaboration between IE and ITU. The con-mandrel will first be developed for non-irradiated specimens (cold-cell) and subsequently transferred for application for irradiated specimens in hot-cells at ITU.

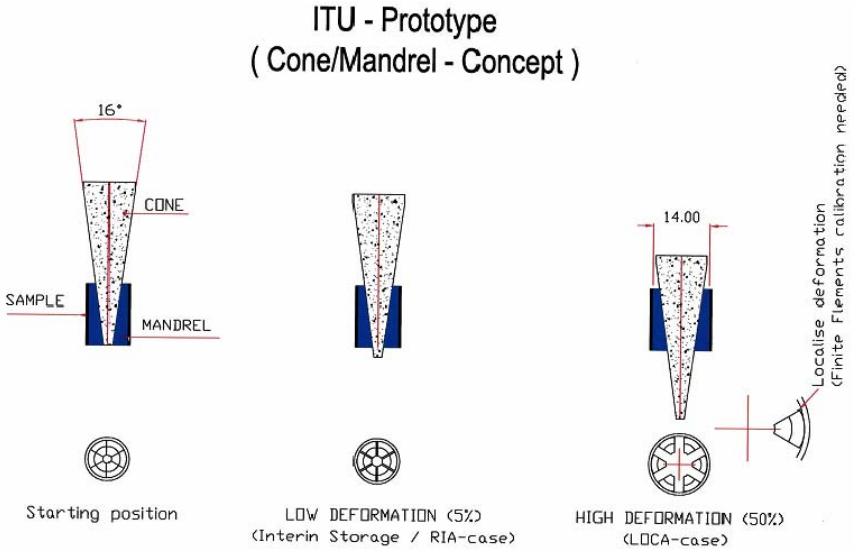

Figure 2 Schematic illustration of the principles for the Mandrel test.

The Mandrel test development at IE started in the second half of 2007. The main objectives in the first part of this development work was a) to design the test and perform scoping test at the IE structural integrity test labs b) to study by finite element analysis how basic design parameters such as number of segments and shape of the cone affect the strain variation in the cladding tube. This Technical Note summarizes some preliminary results.

Description of the Mandrel Test device

As mentioned above the Mandrel consists of a set of arc-shaped segments placed inside a section of a Zircaloy tube and pushed outwards by the vertical displacement of a conical shaft. The practical implementation of the test was done for a Mandrel with eight segments. During the execution of the test, load, displacement and diametric strain were registered. Figure 3 shows the Mandrel test device.

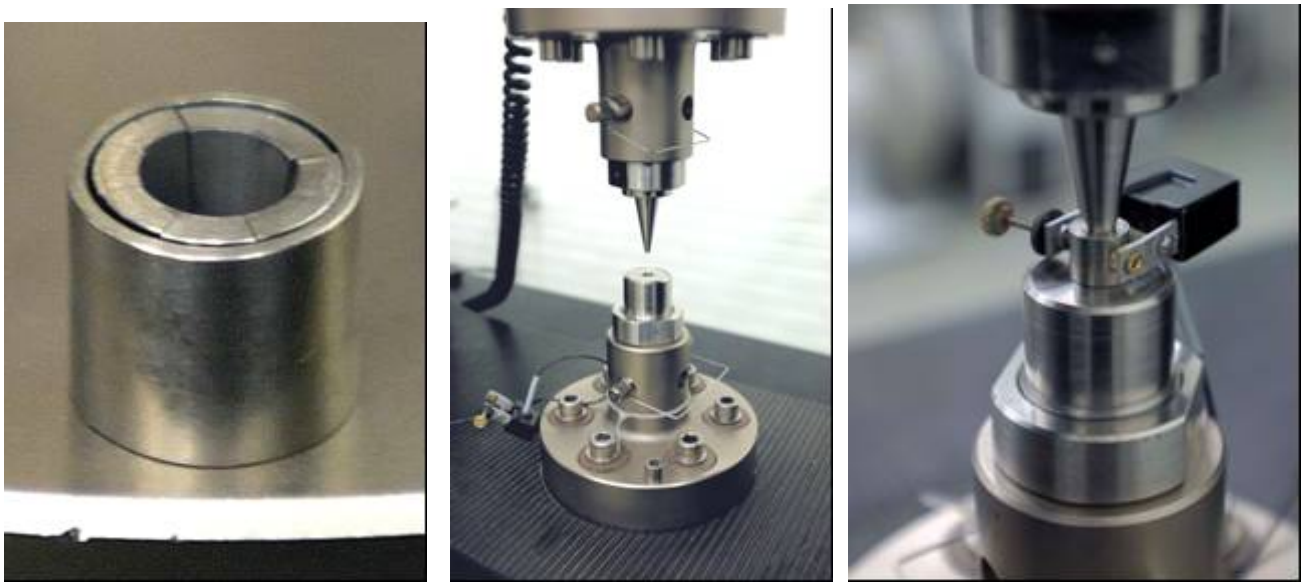

a) b) c)

Figure 3 The Mandrel test device a) cladding tube with segments b) loading device with cylindrical block, cone, segments and cladding tube c) loaded specimen with extensometer for strain measurement

The designed prototype for the experiment consists of a lower cylindrical block, a cone and a set of eight segments. The cylindrical block and the cone were machined in AISI 316 stainless steel. The angle of the cone is 20º. The lower block has a hole with a diameter suitable to allow enough travel for the cone to move down into it, whilst still providing a sufficient base to maintain the assembly of segments and tube in position. Both pieces are pin-held on the load frame tightened with nuts after fine alignment.

The segments are made of Nimonic105. Two sets of segments were prepared for different tube geometries. The segments were machined from cylindrical pieces with diameters equal to the inner dimension of the tubes. A central hole was machined away in the cylinders to have a surface that matches the shape of the end section of the cone. A small slot was also machined from the outer part of the cylinder. The segments were subsequently cut into the eight nominally identical segments. The purpose of the slot is to accommodate a wire spring that should hold the assembly together. This element was however not employed during these trial tests. The cone, the segments and the inner surface of the cladding tube were covered with a lubricant to minimize friction between the parts.

Figure 4 Machined segments and zircaloy tube.

The load frame was an electro-mechanical test machine Instron 5586. The transducers were a load cell 2525-114 with a capacity of 300 kN, and a transverse strain extensometer 2640-008 (travel 2.5 mm) The extensometer was mounted with a special contact device to achieve a firm setting on the tube's surface. The test control and data acquisition was performed with the software console Bluehill2 with the sampling rate set to 1 second.

Test Results

Mechanical Test

Three specimens of non hydrogen-doped Zircaloy were tested as first exploratory trials for the practical implementation of the experiment. The Table below summarizes the specimen dimensions and the loading procedure for the three trial tests.

Table 1: Test Matrix and summary of

Test #	Material	Specimen dimensions			*Loading*
		Outer Diameter, Ø (mm)	Wall thickness, t (mm)	Height, H (mm)	
1	Zircaloy – unknown type. This tube was provided by ITU.	11.10	0.75	9.60	*Compressive load up to 7.6 % strain with a constant displacement rate of 0.284 mm/min.*
2	Zircaloy 2	10.74	0.74	9.60	*This specimen was tested in two stages. A fist load cycle load until 1.2 % strain, followed by an unload ramp (2a). In a second test the tube was loaded until failure (32% hoop strain). Both ramps were executed at a displacement rate of 0.2 mm/min (2b)*
3	*Zircaloy 2*	*10.74*	*0.74*	*9.60*	*Increasing load cycles applied with a displacement rate of 0.2 mm/min.* *The unloading points were set at displacements of 0.3, 0.5, 1.0, 2.0 mm and successive increases of one millimetre, until failure, which occurred at 24% hoop strain .*

The measured hoop strain and reaction force versus the applied load on the cone are plotted in Figure 5, 6 and 7 for the Test #1, 2 and 3 respectively. For each Test there are three plots: reaction force vs. applied displacement; hoop strain versus applied displacement; and hopp strain vs. reaction force. The hoop strain for an applied vertical displacement u_z is given by $\varepsilon_\varphi = u_r / R = u_z \tan(\varphi) / R$, where φ is the cone angle. The slope, $\Delta\varepsilon_\varphi = \Delta u_z \tan(\varphi) / R$, is indicated with a black line in the hoop strain vs. applied displacement plots.

The first Test was only loaded to 7.5% strain. Apart from the initial displacement the hoop strain follows the linear equation quite well. The tube yields at about 1% strain and for higher strains the load remains constant indicating a more or less non-hardening behaviour or even slight softening.

Test # 2 was first loaded to a vertical displacement of 0.9 mm which resulted in 1.2% strain and then unloaded. According to the hoop strain formula above, the strain increment should be 3.5% per mm applied vertical displacement. For the loading part it is quite clear that the strain does not increase linearly with the load and the initial strain is lower than given by the formula. This could be caused by non-perfect alignment. The unloading is also quite complex. The reaction force first drops drastically from 8 kN to 1 kN as the applied displacement is lowered from 0.9 to 0.8 mm. When the load is further reduced there is some elastic unloading. The plastic residual strain is 0.6 %. The load-strain curve for the second load cycle is shown in Figure 6b, d and f. A load maximum is achieved at about 27% strain. This load maximum indicated that there is a kind of “necking” behaviour with localized plastic deformation. The load then decreases as the strain is further increased and the tube cracks at about 33% strain. The onset of necking and the failure are indicated in the plots.

For the third trial test (Test #3), the tube was loaded and unloaded several times. The unloadings did not result in any measurable strain reduction. From the load-strain curve it appears that the unloadings did not affect the overall behaviour. It can be noted that Test # 3 had significantly more hardening that Test #2. For instance at 20% strain the force on the cone is about 16kN for Test #3 but only 12 kN for Test #2. The load maximum also occurs for 16 kN and the failure is at about 24% strain.

The load displacement curves for the three tests are plotted together in Figure 8. This suggests that the global stress-strain curve is affected by the loadings and un-loadings.

The complex unloading behaviour is not so easy to interpret. One explanation to the observation that the measured strain does not decrease when the cone is unloaded is that as the tube deforms plastically, and with higher deformation when there is a gap between the segments, the segments stick to the tube. This is a bit similar to a piece of material that is inserted into clay. Even after complete unloading it was virtually impossible to separate the segments from the tube. A second explanation is that there is relatively strong friction between the anvil and the segment and the cylinder, and that this friction must be overcome before the tube and segments can separate. The sudden reduction for the load cycle for Test #2 indicates such behaviour.

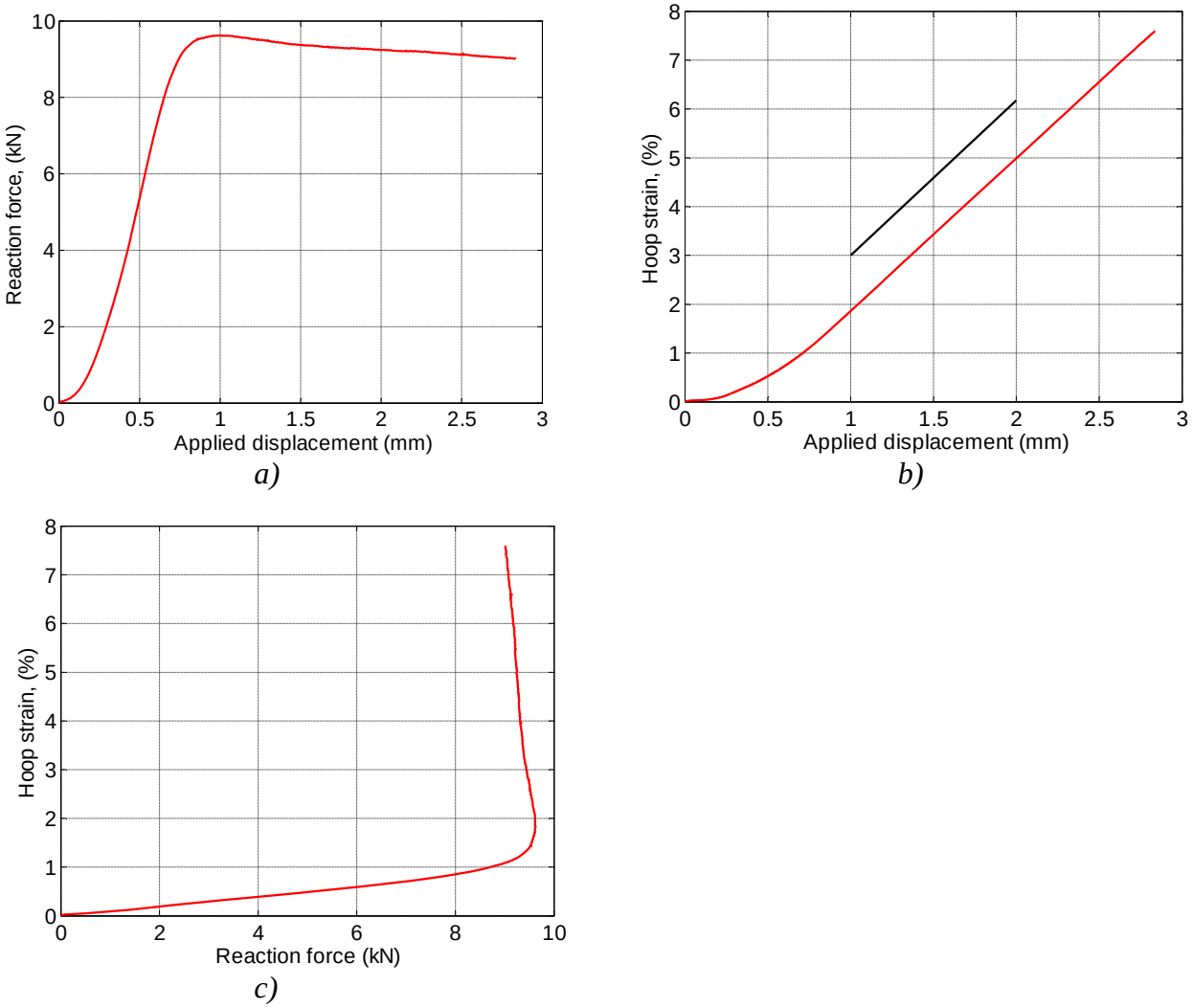

Figure 5 Test #1 a) Measured reaction force vs. applied displacement b) measured hoop strain versus applied displacement c) measured hoop strain versus measured reaction force

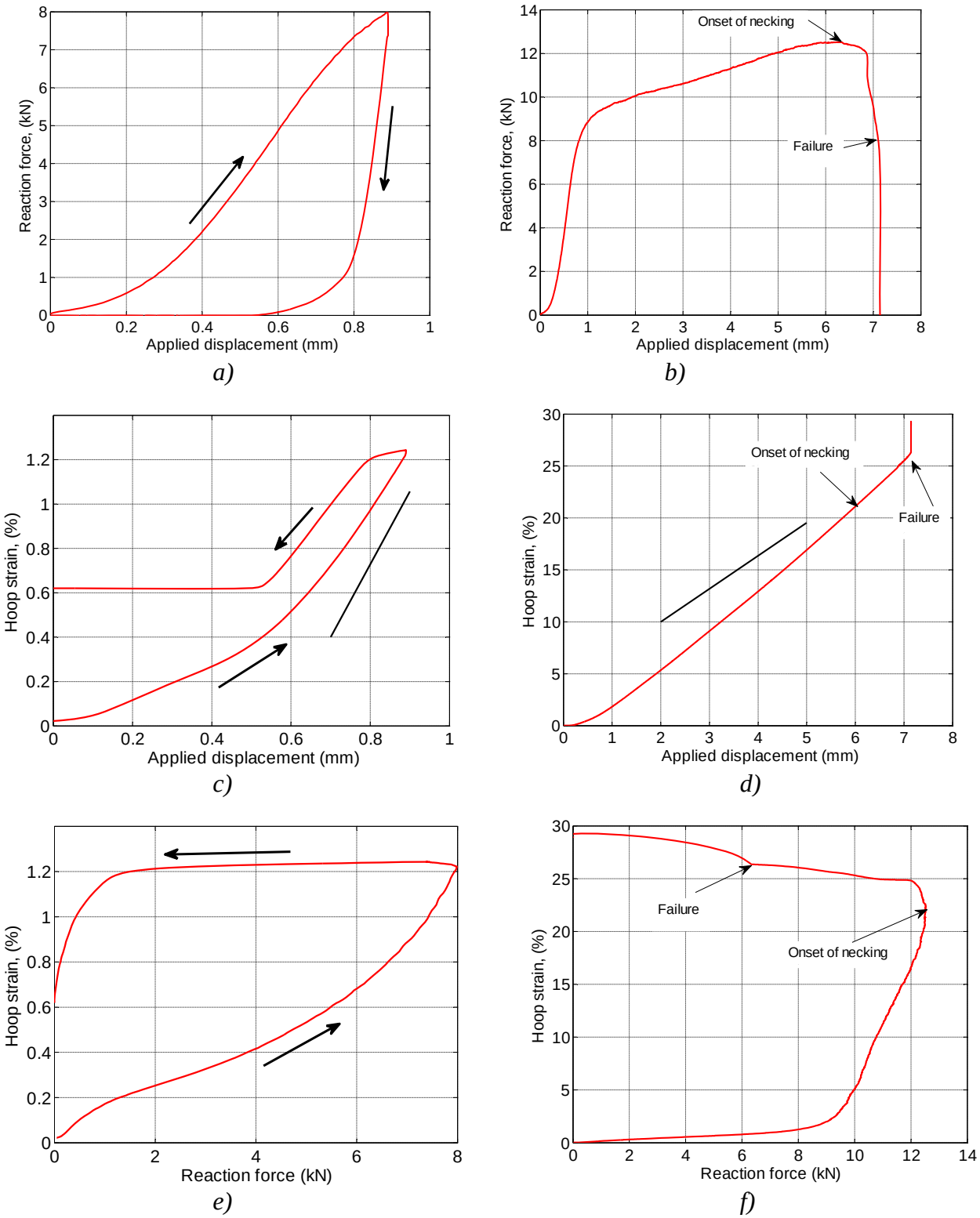

Figure 6 Test #2 a) and b) Measured reaction force vs. applied displacement c) and d) measured hoop strain versus applied displacement e) and f) measured hoop strain versus measured reaction force

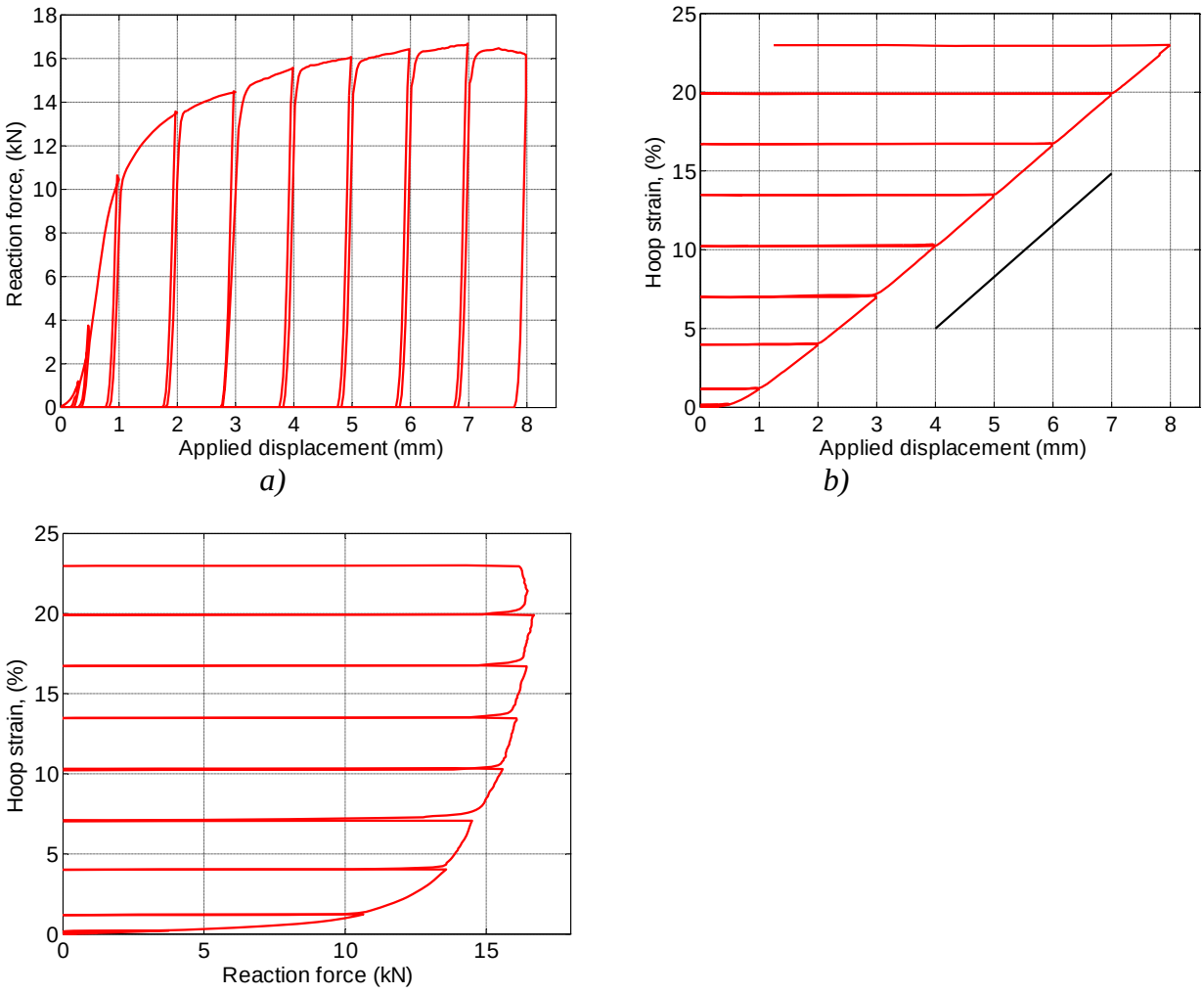

Figure 7 Test #3 a) Measured reaction force vs. applied displacement b) measured hoop strain versus applied displacement c) measured hoop strain versus measured reaction force

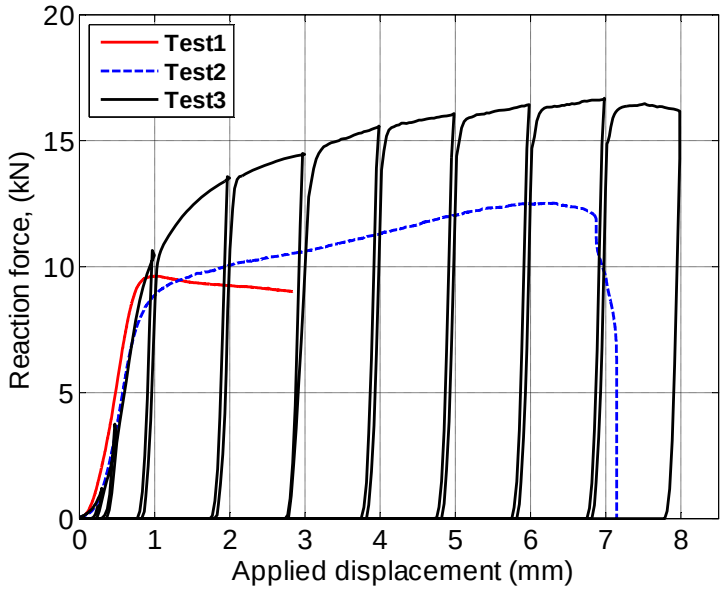

Figure 8 Measured reaction force vs. applied displacement for the three tested specimens

Post test analysis of cladding tubes

The fracture behaviour of two specimens for Test #2 (here also referred to as Zyr4A) and Test #3 (Zyr4B) was analyzed by Scanning Electron microscope (SEM), using secondary electron imaging and X-ray dispersive analysis (EDX). As the behaviour of the two tests was very similar the observations from the structural analysis will be discussed jointly. Figure 10 to 21 are taken from Test #2 whereas the Figures 22 to 24 refer to Test #3.

As mentioned above the Mandrel test loading resulted in local thinning, necking and cracking as seen in Figure 10 and 22 for Test #2 and Test # 3 respectively. The cracking of the specimens was influenced by shear stress as expected and took preferential direction of 45° angle (Fig 10, 11, 22). Cross slip at the middle of the crack is also visible.

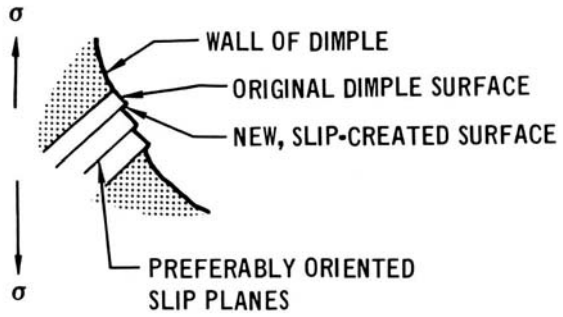

Figure 9 Schematic illustration of slip bands

Radial and axial shear bands are present on outer surface of locally thinned area and are described on Figure 11, 15, 21, 23 and 24. The largest shear stresses occur in bands that make an angle of 45° with the hoop stress. New slip-created surfaces are present on the shear band planes (Figure 16 and 17). Such shearing and the corresponding deformation results in stress concentration in local areas and at some stage resulted into fracture starting in the point of origin shown in Figure 21. The dominating fracture mechanism was transgranular ductile tearing/shearing, or dimpling (Figure 12, 18). The EDX analysis indicated that the dimples appear to have originated from randomly segregated Al, Fe, Cr rich particles that were embedded in matrix (Figure 13). As the load is increased microvoids in the material (Figure 12) grow, coalesce and eventually form fracture surfaces. The slip step formation causes serpentine glide and ripples on a dimple wall as shown in Figure 19.

The shape of the dimples is strongly influenced by the stress state acting on the material. Fracture under uniaxial stress results in the formation of equiaxed dimples in the hoop direction (Figure 15), which was the case of the end of fracture process – fracture tip. Shallow dimples are defined by less plastic deformation of material and more conical dimples by more pronounced plastic deformation material which is the case for the two analyzed specimens.

If the shape of dimple is elongated or parabolic it means it resulted from shear loads. In our case dimpling present on the crack oriented in 45 degrees is elongated and therefore dimples corresponding to shear (Figure 18), because the opposite fracture surface dimples are oriented in opposite direction which is the case only for shearing – tearing has dimples oriented in the same direction. However it still indicates the position of the point of origin as it is in this case. Point of origin was present in the very edge of the sample and is recorded in Figure 21 and 24 for Test #2 and Test #3 respectively.

ZYR 4 A:

Figure 10: 3D, front, left and top overview of tested Zyr4A specimen. Crack together with local resulting from deformation is present. Mandrel test device pattern is visible inside of specimen.

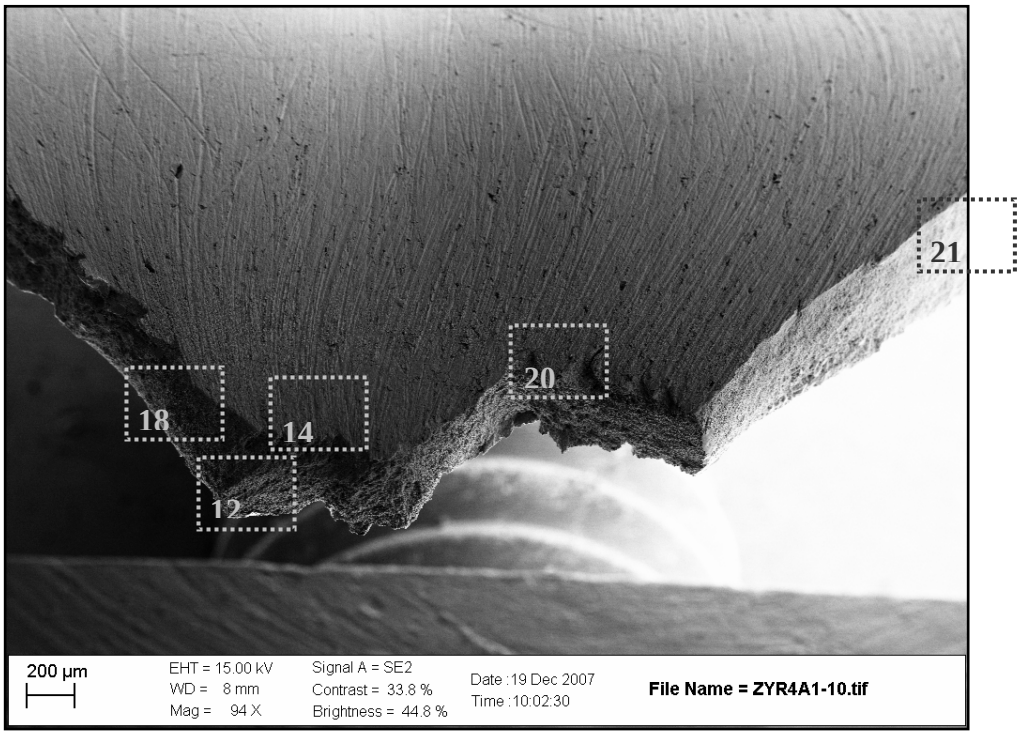

Figure 11 Zyr4A fracture. Inserts are describing a position of following figures. Discoloration in r necking (visible in Figure 10 - light) corresponds to radial shear bands, now nicely visible forming 'rou 'scratchy' surface.

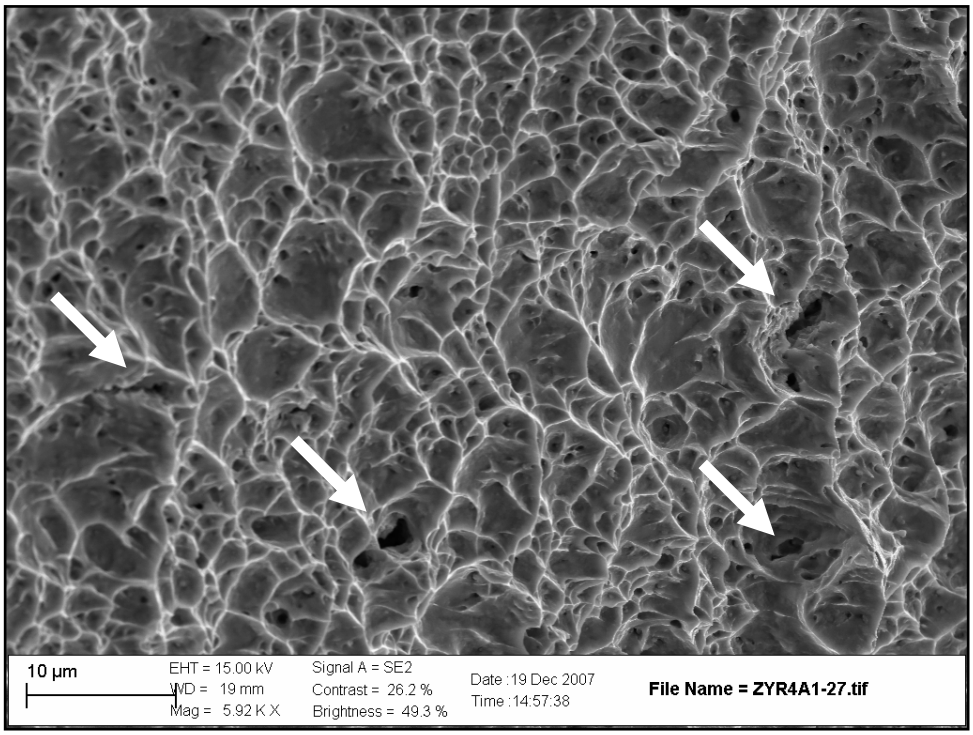

Figure 12: Ductile tearing is dominating fracture mechanism. Voidation is out pointed by arrows.

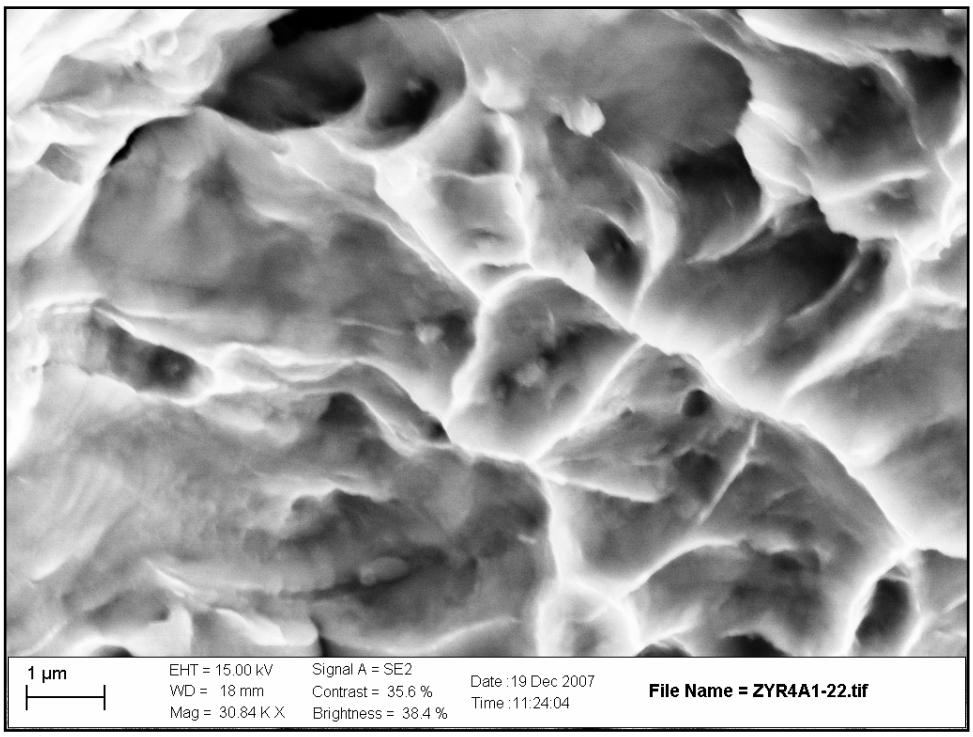

Figure 13 Al, Fe, Cr rich particles embedded inside of a deformation crater indicating the starting ductile shearing process.

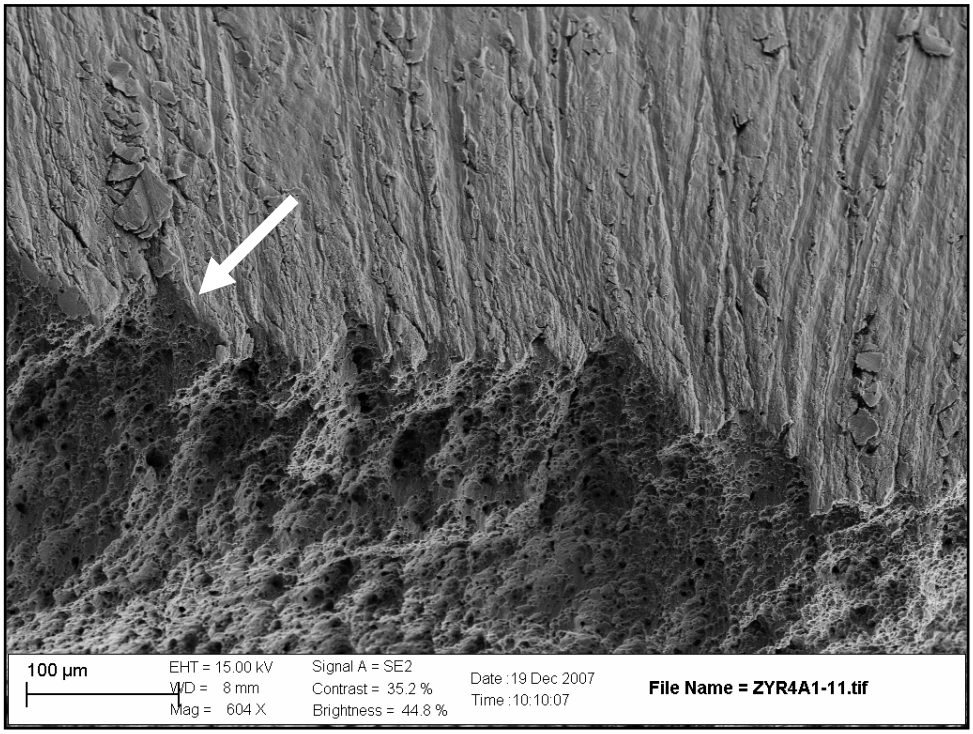

Figure 14 Teeth like shape of the edge of the fracture surface.

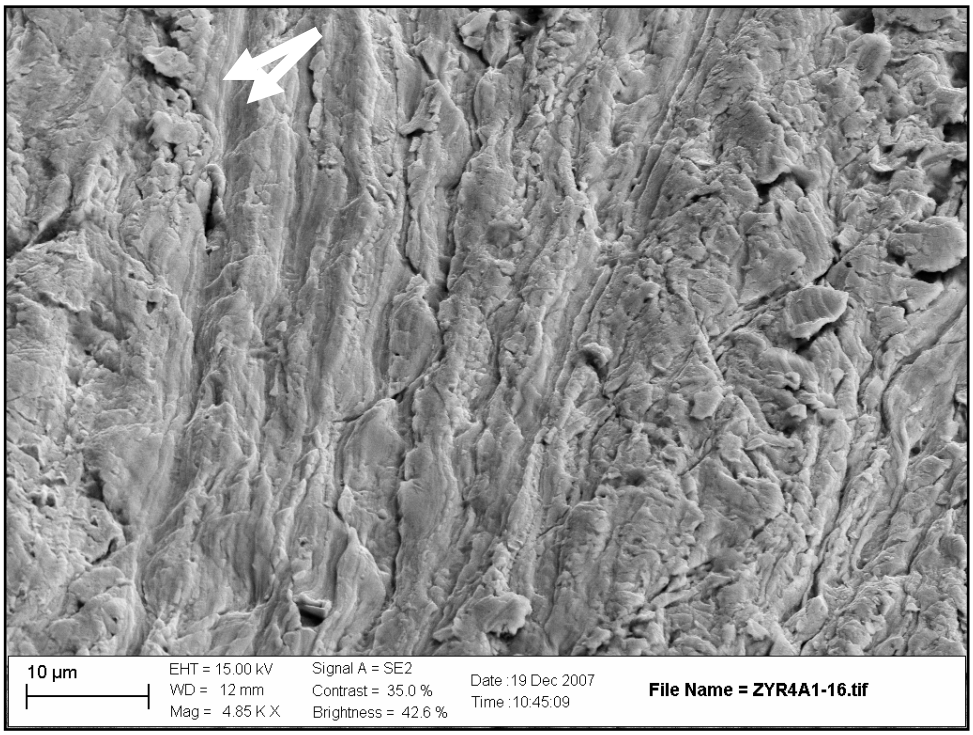

Figure 15: Closer view on surface deformation shear bands indicating slip plane mechanism of defo view of slip plane edges is presented on next figures – Figure 16, 17.

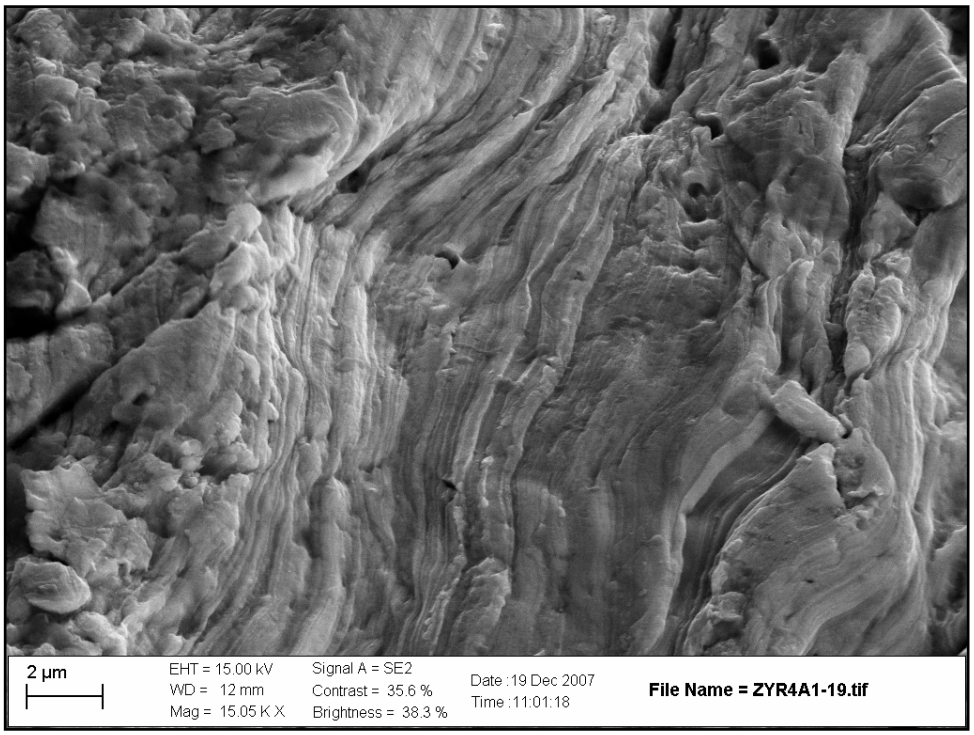

Figure 16 One of the detailed views on the surface deformed zone – shear bands. Picture is presen planes effecting from deformation of specimen.

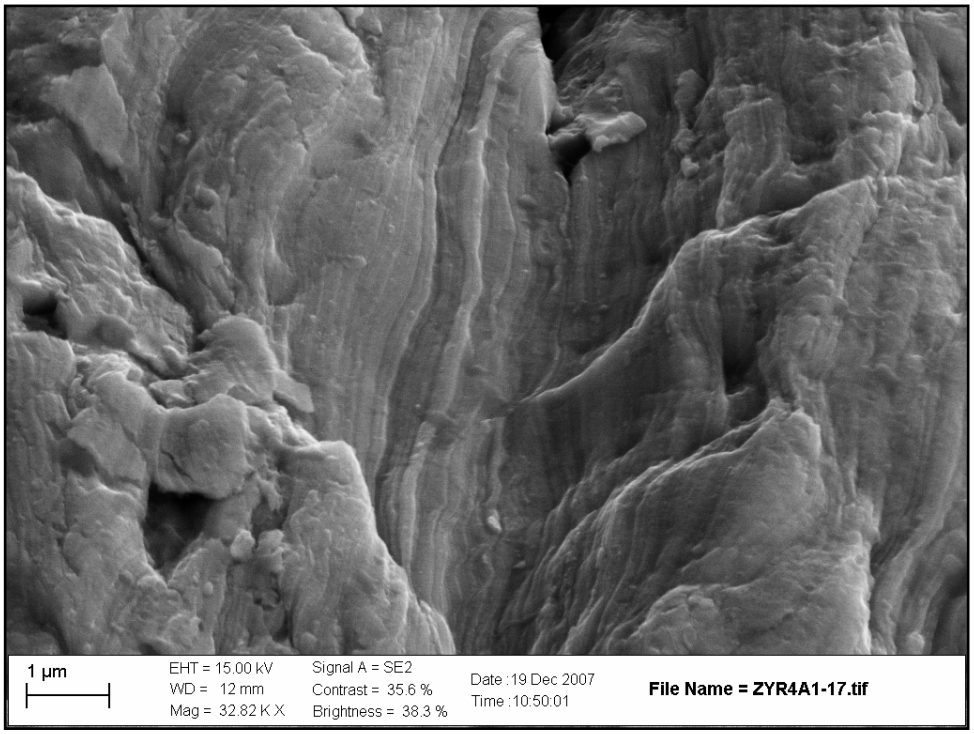

Figure 17 One of the detailed views on the surface deformed zone – shear bands. Picture is presen planes effecting from deformation of specimen.

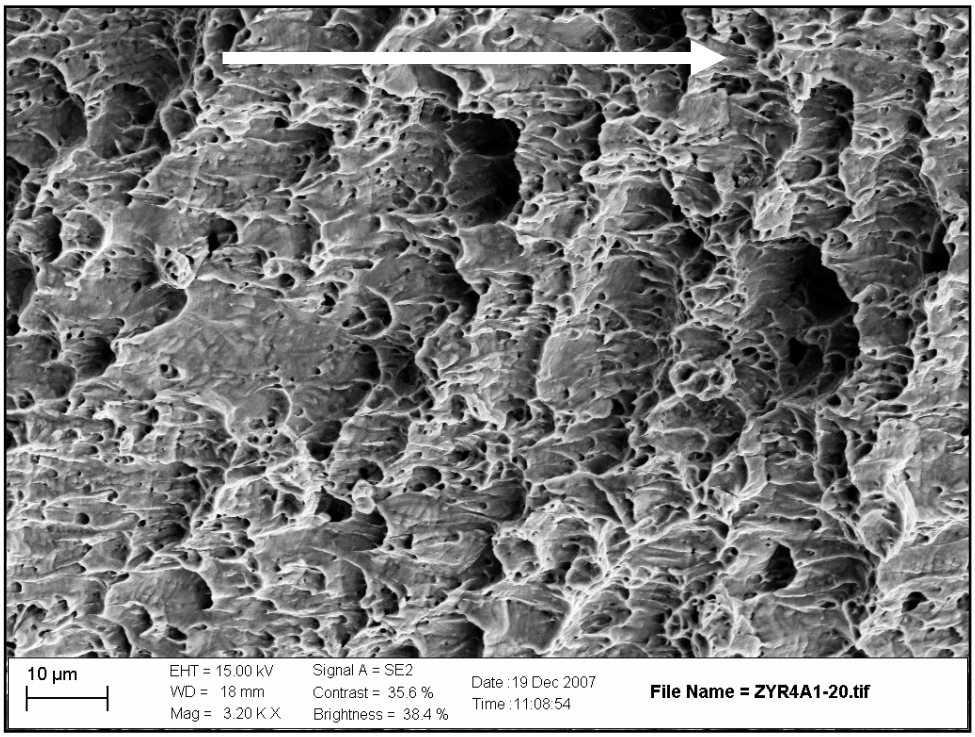

Figure 18: Ductile tearing on the side of fracture is affected by the 45^{o} dominating direction. Arrow is direction of the fracture propagation.

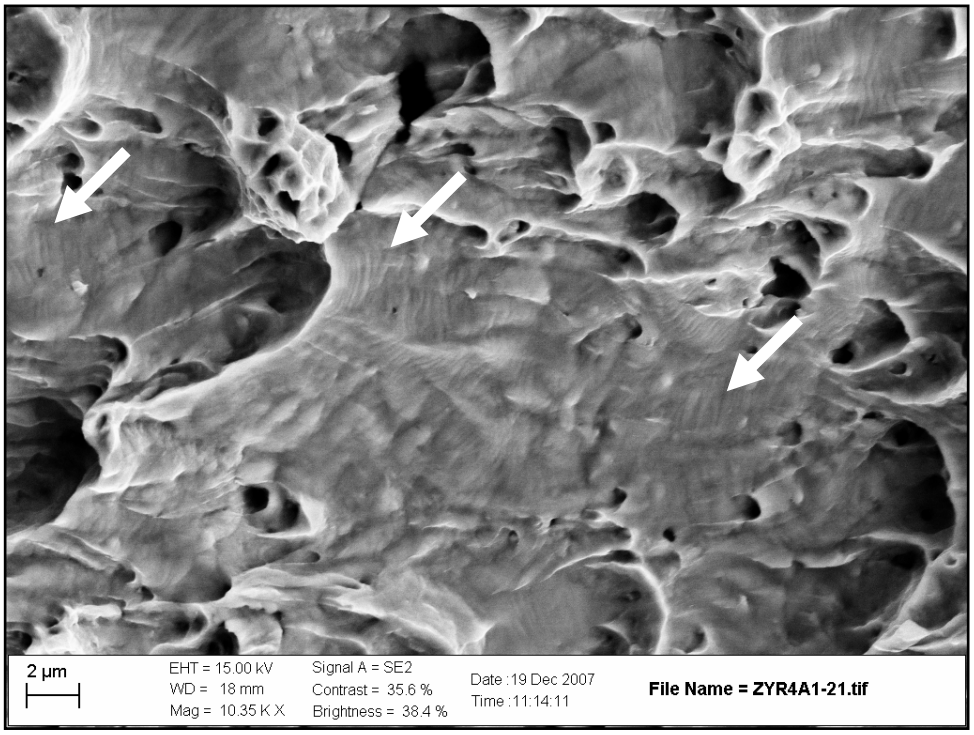

Figure 19: New, slip-created surfaces on the fracture surface presented in Figure 18.

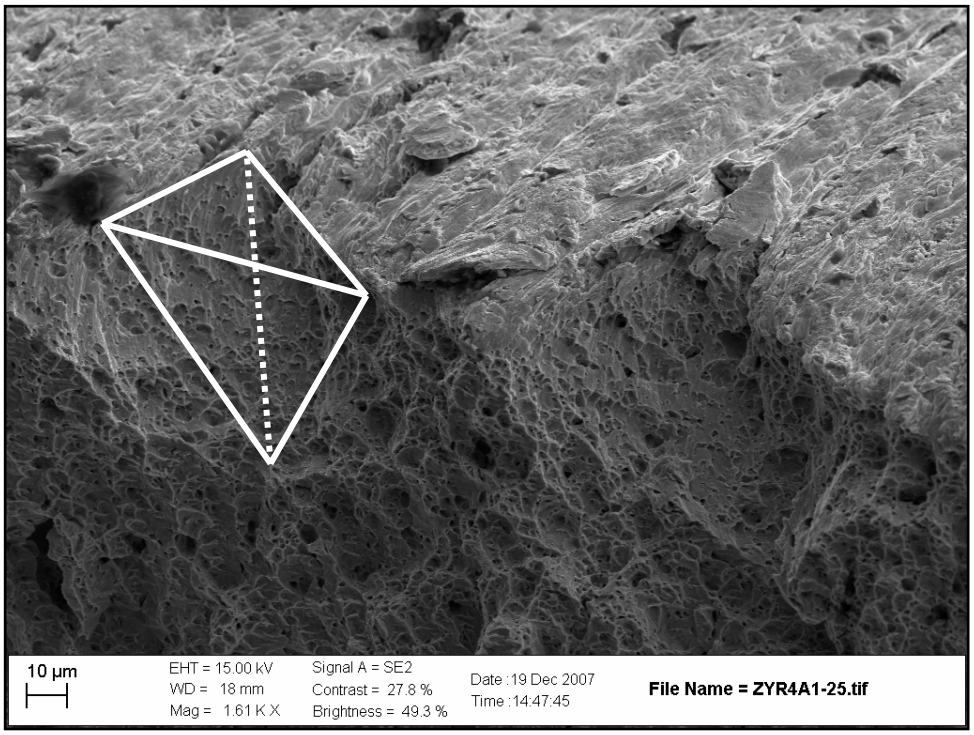

Figure 20 Detail of the teeth like edge of fracture surface. Triangle holes resulting from five dominatin and/or boundary zones connecting at the end of fracture.

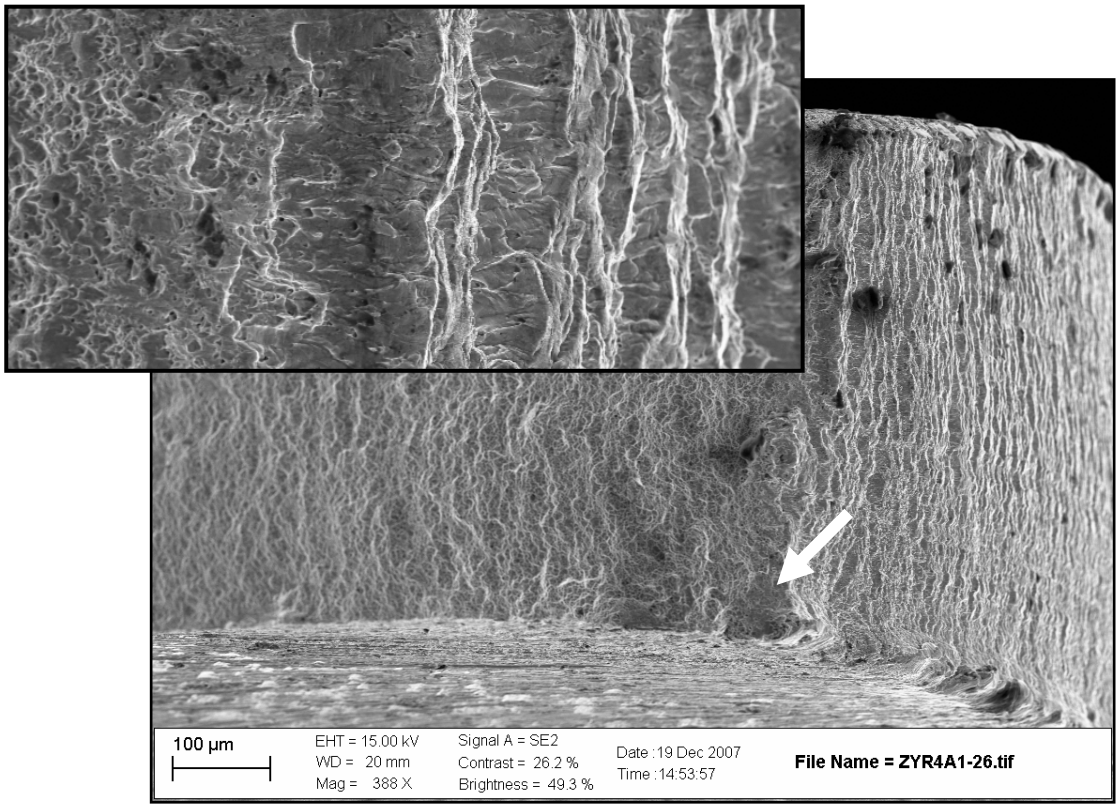

Figure 21 Far right (left) side of the fracture surface with beginning of the fracture – point of origin (ar slope and inserted detail you can see slipping planes resulting from deformation and thinning of specime

ZYR4B:

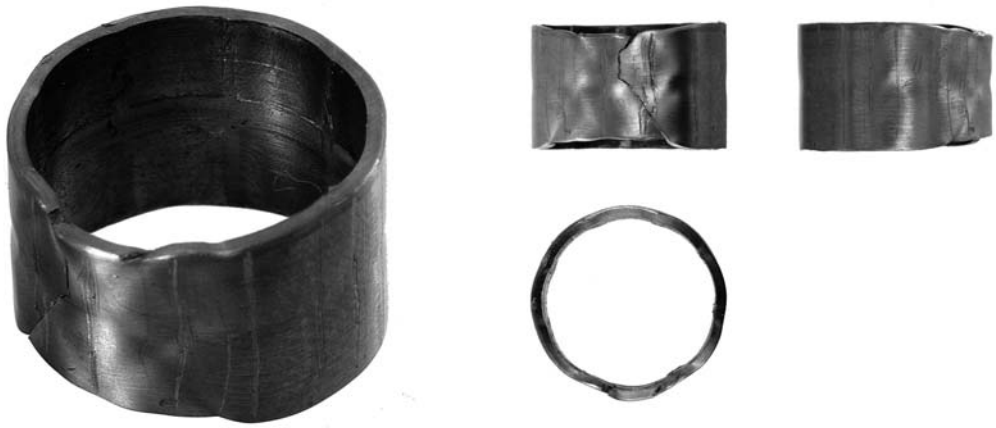

Figure 22: 3D, front, left and top overview of tested Zyr4B specimen. Crack together with local necking deformation is present. Mandrel test device pattern is visible inside of specimen.

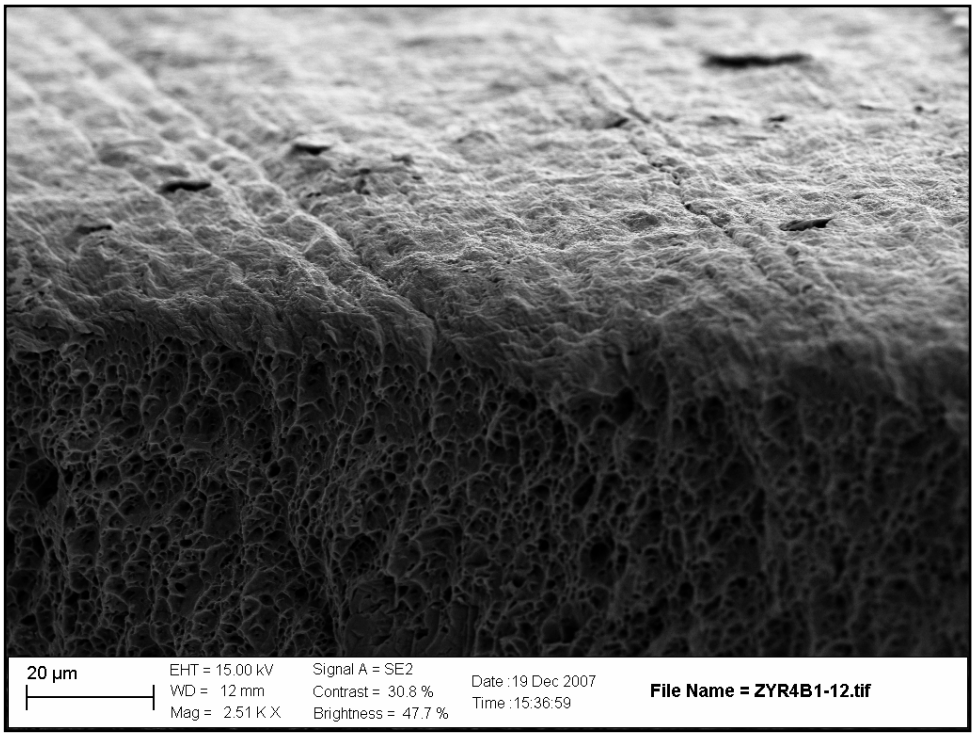

Figure 23 Closer view on surface deformation skips indicating slip plane mechanism of deformation. Sa described in Figure 12 and detailed in Figure 13, 14.

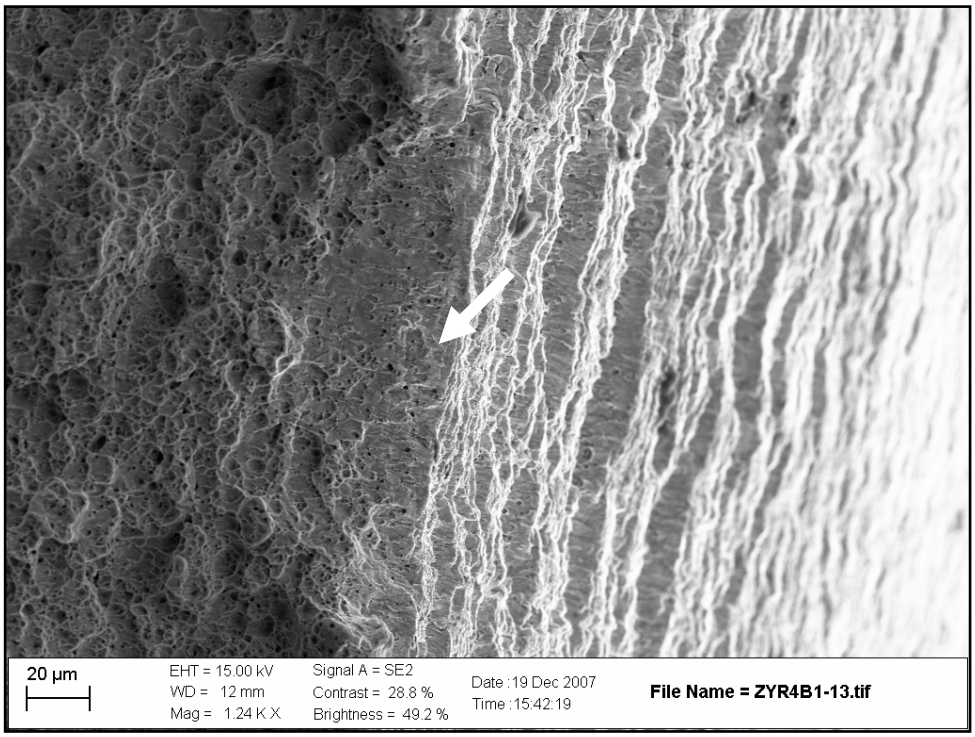

Figure 24 Point of origin (arrow) and slipped planes as described in Figure 21 are also present in Zy same area.

Supporting FE-Analysis

Model description

The Mandrel tests were analysed by finite element calculations. Figure 25 shows the FE model and associated boundary conditions for the Mandrel with eight segments. Due to symmetry only half a segment needs to be modelled. The model is two dimensional (2D) plain strain with a uniform and fine mesh for the cladding tube. The segment has the same mesh refinement as the tube along its outer radius but the mesh is coarser away from this region. The tube and segment are modelled as elastic-plastic materials. Table 2 shows Young's moduli and Poisson's number for the two materials involved and Figure 26 the associated stress-strain curves. The stress-strain curve for the Zircaloy-2 was provided by AREVA NP GmbH whereas the segment material Nimonic 105 data was taken from literature.

The interface between the segment and the cladding tube is modelled by Coulomb contact analysis with a coefficient of friction equal to 0. A radial displacement, Ur, is imposed on the segment's inner-surface. As will be discussed below it is difficult to achieve numerical convergence at high loads woth onset of necking and the maximum displacement applied for the eight-segment case was 1.7 mm. The segment is very rigid compared to the tube and the tube will also have, more or less, the radial displacement, Ur. The nominal hoop strain along the inner surface of the tube is therefore $\varepsilon_\varphi = U_r / R$ and the maximum value is thus 1.7 / 5.0875 = 33.42 %.

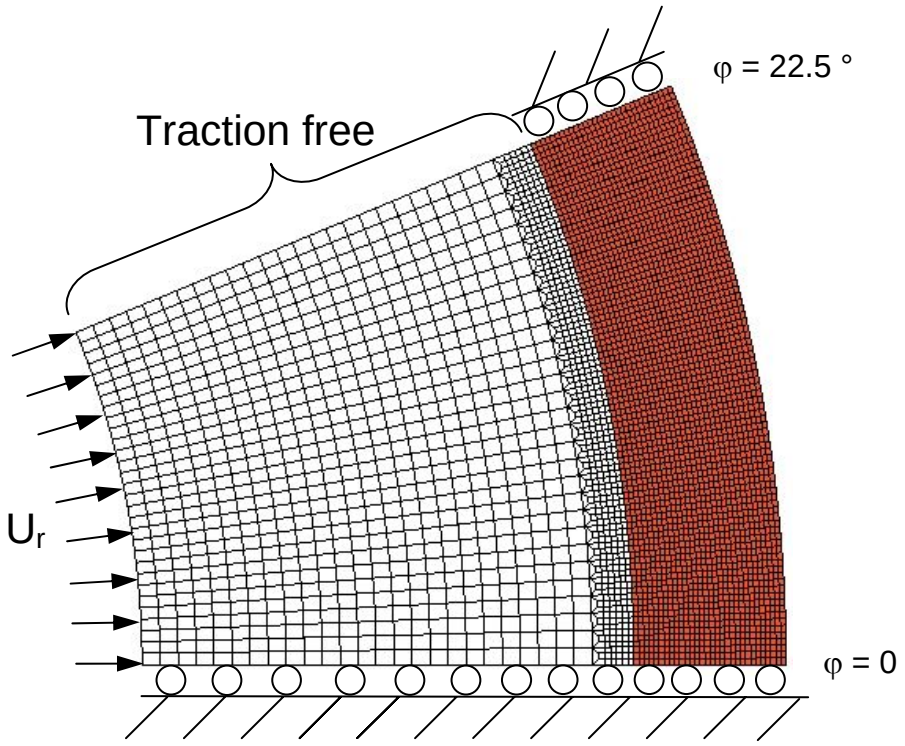

Figure 25: The finite element and associated boundary conditions model for the 8-segment mandrel and tube

Table 2: Elastic material properties

Material	**Zircaloy 2**	**Nimonic 105**
Young's Modulus [N/mm^2]	100,500	220,000
Poisson Ratio	0.3	0.3

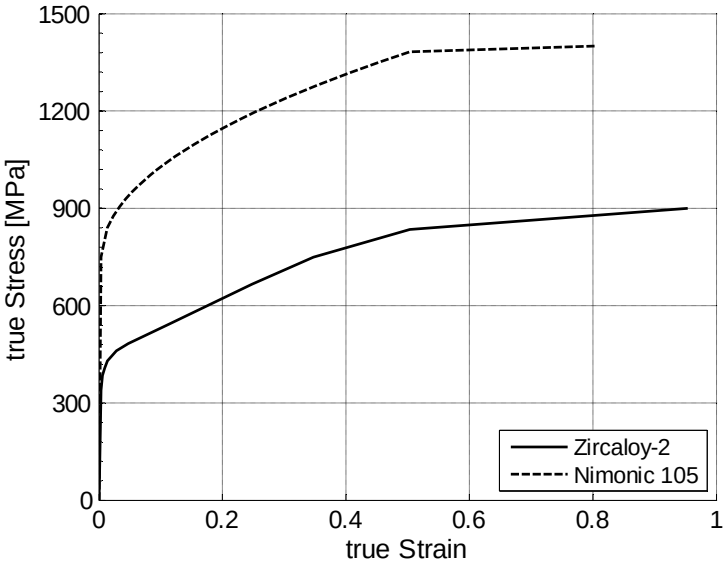

Figure 26: Stress-strain curves of Zircaloy-2 and Nimonic 105.

Results

Comparison computed and measured data for 8-segment Mandrel

Figure 27a and b show the computed hoop strain on outer edge of the tube at φ = 0 for an applied radial displacement of U_R = 0.0611 mm and U_R = 1.7 mm respectively together with the measured values from Figure 6 and 7. The displacement corresponds to the axial displacement, $U_z = U_R / \tan(\varphi/2)$. The computed curves give of course a linear relationship for loading and the elastic unloading. As discussed in previous sections the measured strain does not increase linearly with the displacement for low loads, and for low loads the measured strain is smaller than the computed values. As already mentioned this is probably caused by a gap between the cone and the segment and non-perfect alignment of the cone and tube. By translating the applied displacement in the computed curve by 0.5 mm a better agreement with the measurements is attained as seen in Figure 27a. This indicates that the gap is $0.5 \cdot \tan(\varphi/2) \approx 0.09 mm$.

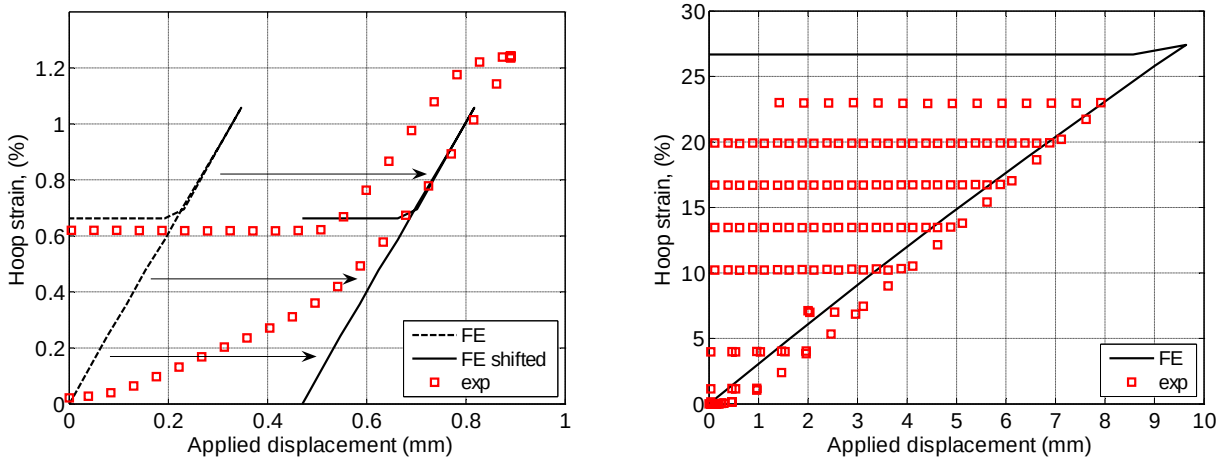

Figure 27: Hoop strain for applied radial displacement of a) 0.0611 mm experiemtal data from Test #2 and b) 1.7 mm and experimental data from Test #3.

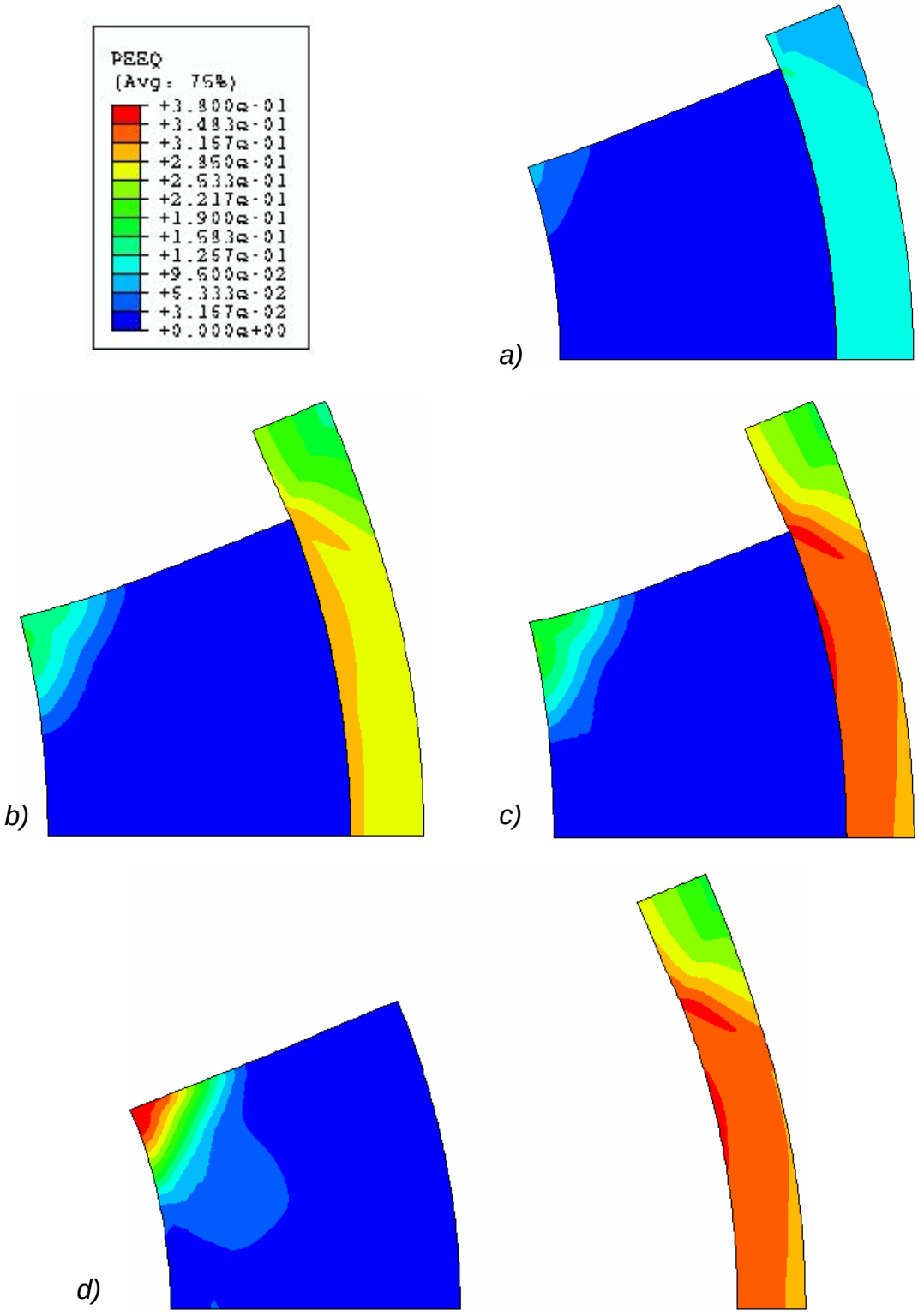

*Figure 28: Strain iso-contour plots at a) U_r = 0.33*1.7mm load, b) U_r = 0.83*1.7mm, c) U_r = 1.7mm and d) after unloading.*

Figure 28 shows iso-contour plots of the equivalent plastic strain at Ur = 0.33*1.7 mm, 0.83*1.7mm, and 1.7mm and after complete unloading from 1.7 mm. As expected the strains are larger on the inner edge of the tube than on the outer edge. A strain concentration that increases with the applied load is clearly seen in the tube at the end of the segment. The unloading is elastic and the residual strains after unloading are therefore similar to the strains during the maximum load. Noticeable is also the high strain concentration at the inner edge of the segment at its free end, indicating considerable plastic deformation of the segments during test. The residual equivalent plastic strain is in fact significantly higher than at the maximum load. Moreover the strain variation along the inner and outer surface clearly show the deviation from axi-symmetry.

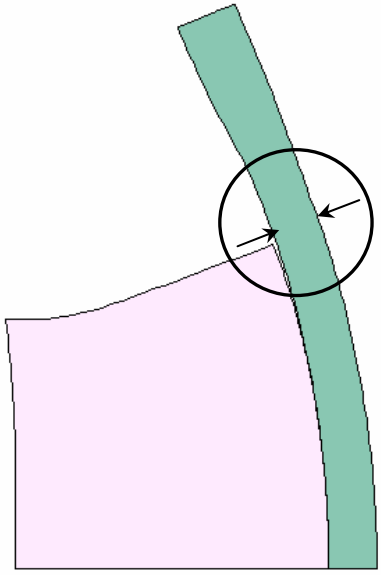

Figure 29: Necking of cladding tube during loading (scale factor 2).

In addition to the strains also the wall thickness varies along the tube segment. Figure 29 shows the deformed tube and segment with a magnification factor 2 for the deformation. Due to the "dominant" hoop stresses the cladding tube contracts in its middle section. Such local thinning-down is referred to as necking and often precedes component failure.

Figure 30 shows the hoop strain vs. the position angle φ along the inner and outer edge of the tube for four different load levels whereas Figure 31 shows the hoop strains vs. the applied displacement at the four angle positions along the inner and the outer edge of the cladding tube. From Figure 31 we note that that the hoop strains have its largest value at φ = 16.25°, which is approximately the position where the contraction is most pronounced at higher loads and where the local strains have their largest values. From Figure 32 we note that for the inner edge at the position, φ = 16.25°, the hoop strain has a strong increase at an applied displacement of U_z = 9 mm. This could be and indication for the onset of necking.

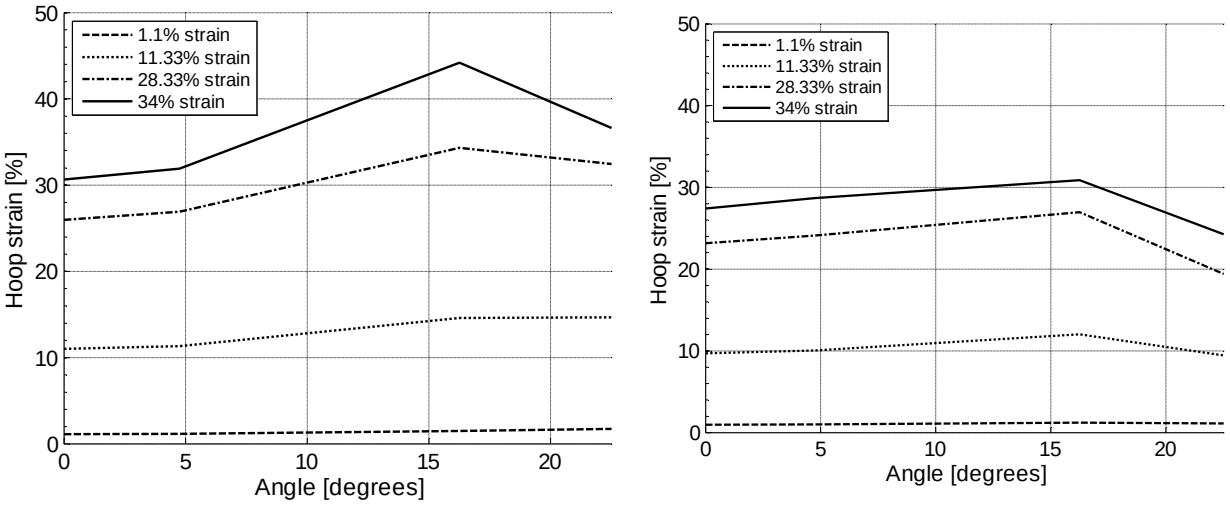

Figure 30: Hoop strain vs position angle for various load levels along a) inner and b) outer edge.

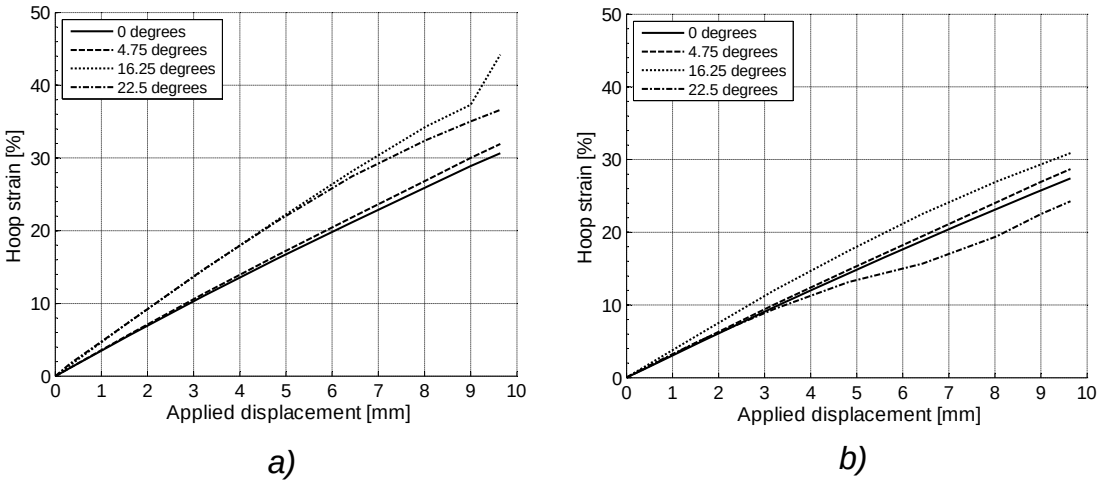

Figure 31: Hoop strain vs. applied vertical displacement at four locations along a) inner and b) outer edge.

Figure 32a shows the wall thickness of the tube normalized to its initial value vs. the applied displacement and Figure 32b shows the normalized wall thickness vs. the position angle for four load levels. As expected the wall thickness decreases with increasing load. The variation in wall thickness along the tube increases with increasing load. The wall thickness has its largest value at $\varphi = 22.5°$, which would be between segments. The location with the local minimum wall thickness shifts slightly with the load but is around 15°.

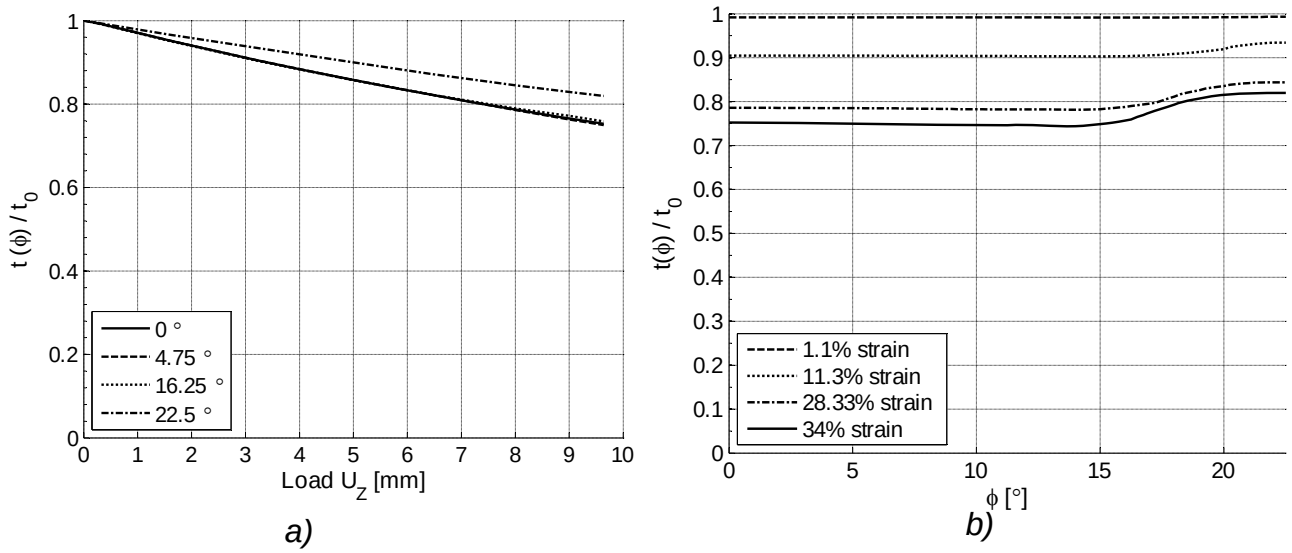

Figure 32: Normalized wall thickness vs. a) load at different position angles and vs. b) position angle at different loads.

Influence of segment's stress-strain curve

Necking is a geometric and numerical instability. Hence it depends also on the tube's stress-strain curve. We saw in Figure 8 that there was a significant difference in hardening between the second and third test. To assess to what extent the necking loads depends on the stress strain curve, the FE analyses was repeated with the reduced hardening shown in Figure 33.

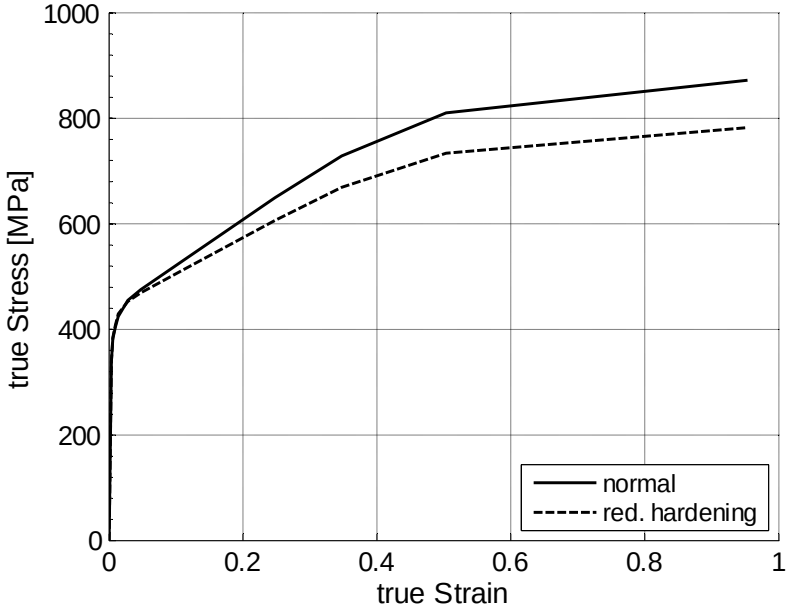

Figure 33: Stress-strain-curves for Zircaloy-2 to assess material dependency on necking.

Figure 34 shows the resulting hoop strain vs. the applied displacement for various positions along the inner and outer edge. The two material models give almost overlapping results. Thus the variation in stress-strain behaviour has virtually no effect on the onset of necking. This can also be seen from the comparisons of wall thicknesses, which are displayed in Figure 35.

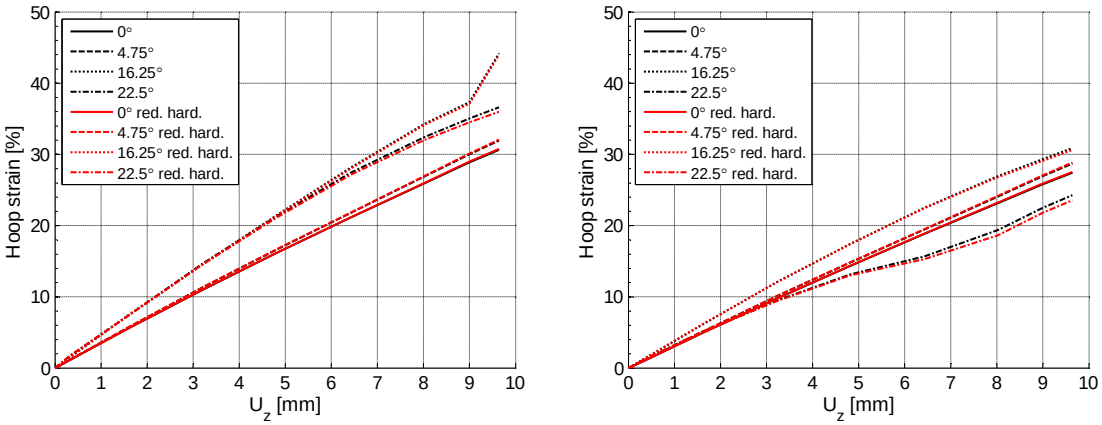

Figure 34: Hoop strain vs applied displacement for various positions along a) inner and b) outer edge with normal stress-strain behaviour and with reduced hardening.

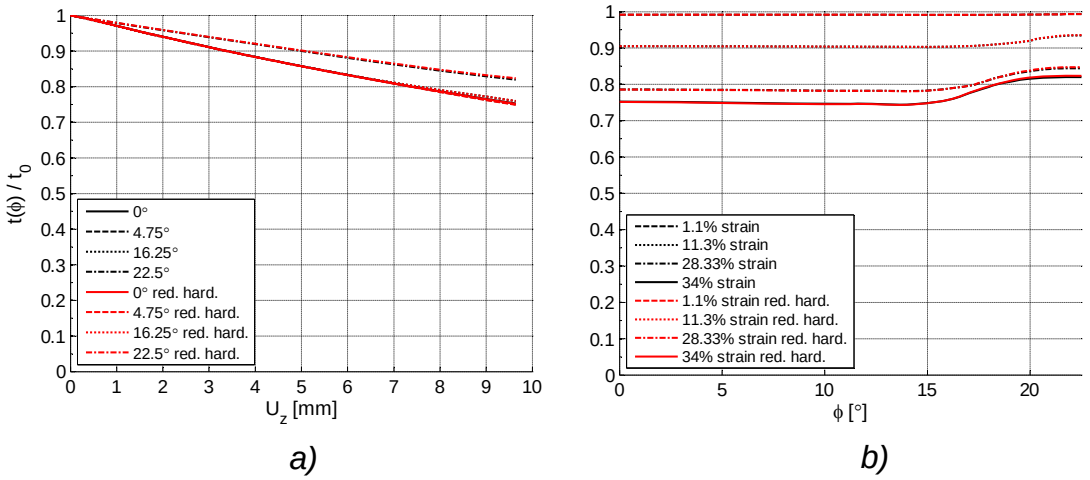

Figure 35: Normalized wall thickness vs. a) load at different position angles and vs. b) position angle at different loads, once with normal stress-strain behavior and once with reduced hardening

Plain strain vs. plain stress

The analyses above are based on plane strain assumptions (i.e. that $\varepsilon_{zz} = \varepsilon_{rz} = \varepsilon_{\varphi z} = 0$). The ends are, however, free to expand so that $\varepsilon_{zz} \neq 0$. This is quite evident from the deformations in Figure 10 and 22. The resultant force in this direction is, however, zero ($\int_A \sigma_z dA = 0$) so for a two dimensional model it could be more natural to assume plane stress conditions (i.e. $\sigma_{zz} = \sigma_{rz} = \sigma_{\varphi z} = 0$) rather than plane strain. The two-dimensional analysis was therefore performed with plane stress as well. Figure 36 shows the computed strains using plane strain and plane stress. The difference is not very large. The main difference is that the peak strain at around 15° is less pronounced in the plane stress case. Problems with numerical convergence was encountered at Uz = 9 mm and no up-shift indicating necking is seen. The convergence problems indicated indirectly necking.

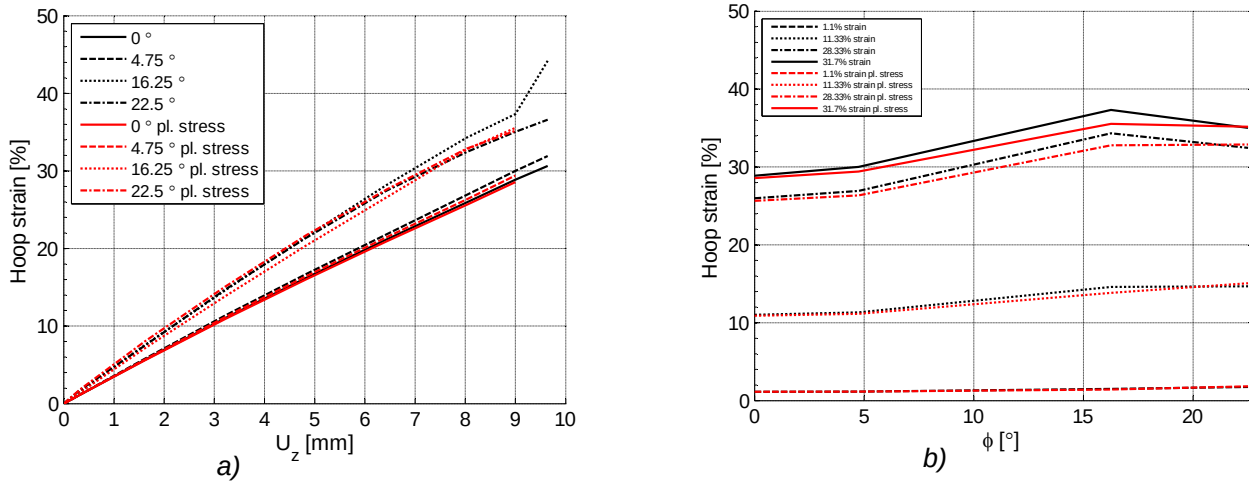

Figure 36: Computed strains from plane strain and plane stress models a) Hoop strain vs. applied displacement for various positions along inner edge and b) Hoop strain vs. angle for different load levels

Comparison 6, 8 and 10 segments for Mandrel

From the FE analyses it is evident that the strain distribution is not axi-symmetric along the cladding tube and that highly non-linear effects and necking are likely to occur at higher loads. For the Mandrel test we want to minimize the strain variation along the tube and increase the load for onset of necking. By increasing the number of segments the strains should become more axi-symmtric. To assess this FE analyses with six and ten segments were also carried out. These FE models were setup in the same manner as the reference model with eight segments in Figure 25 by changing the section angle (30° for 6 segments, 18° for 10 segments). The element sizes are the same in all three models.

Figure 37 shows the ratio between largest and smallest hoop strain along the inner edge of the cladding tube vs. the applied displacement for the different numbers of segments. The maximum loads are those for which numerical convergence could be attained for each case. It can be clearly seen that the strain ratio is highest for the 6-segment Mandrel and lowest for the 10-segment Mandrel. The sudden increase in the strain ratio indicates onset of necking. Hence with this assumption, necking occurs at about Uz = 2, 9 and 11 mm for the 6, 8 and 10-segement models respectively.

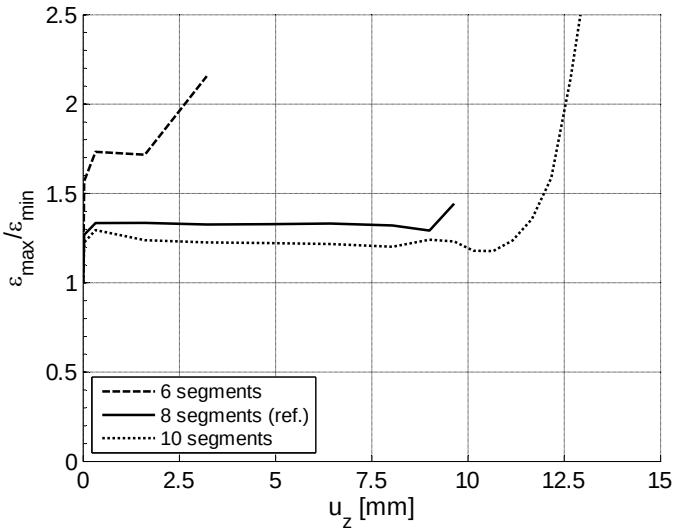

Figure 37: Normalized strain vs. applied displacement for different number of segments.

We saw in Figure 28 that the segment has considerable residual deformation after unloading. Large residual deformations may lead to failure of the segment after repetitive loading and should therefore be minimized. Figure 38 displays strain-iso contour plots of the residual deformation at unloading from U_r = 0.33*1.7mm. The residual strain, overall as well as peak values, decrease with the number of segments in both cladding tube and segment.

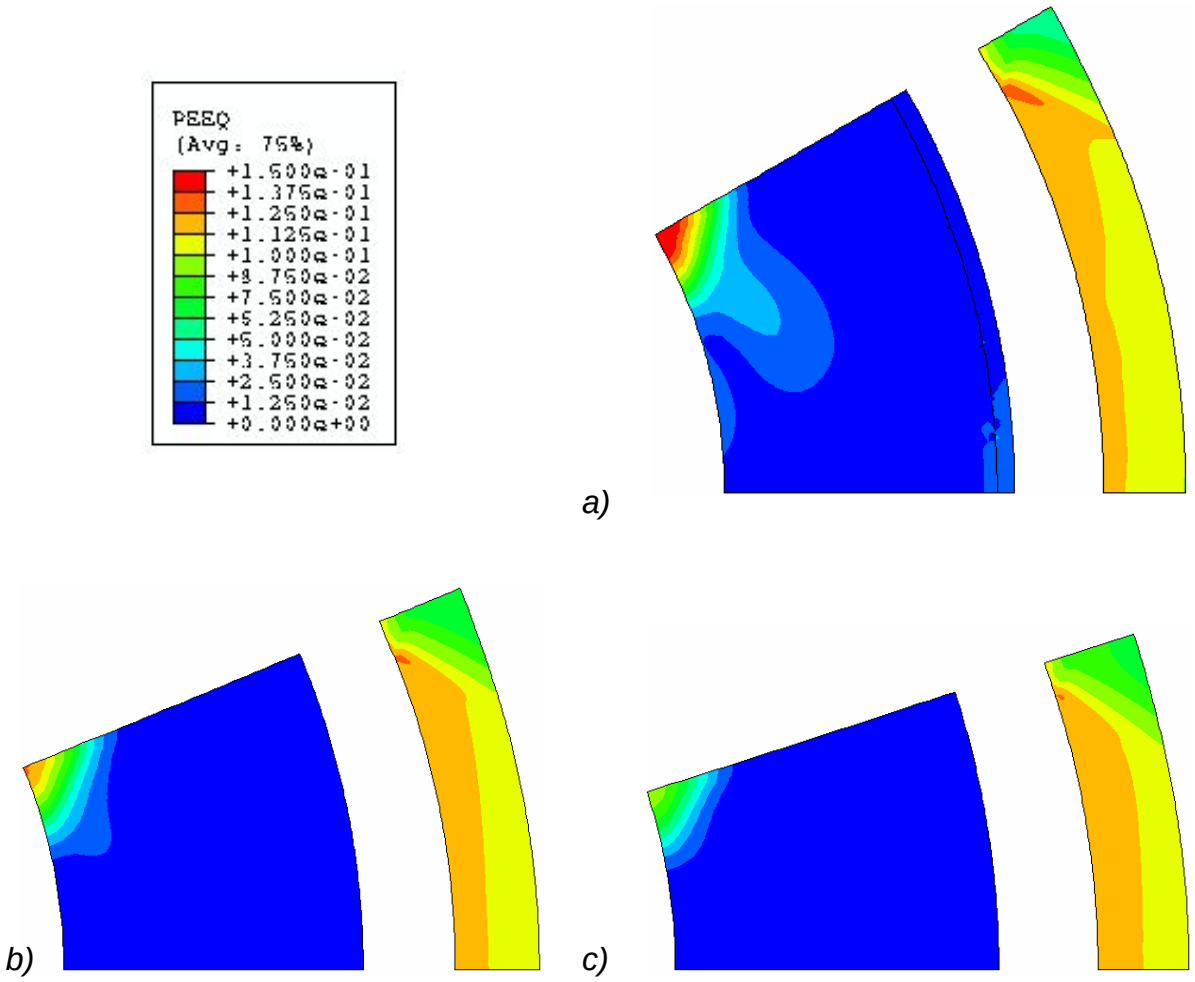

*Figure 38: Strain iso-contour plots after unloading from U_r = 0.33*1.7mm load for a) 6 segments, b) 8 segments (reference), c) 10 segments*

Figure 39 depicts the strain-iso contour plots for 8 and 10 segments at their respective maximum load for convergence. Converged solutions were achievable for loads up to U_r = 1.7 mm for the reference model, U_r = 2.5 mm (U_z = 14mm) in the case of 10 segments, which correspond to 34 % induced strain for the reference model and 50 % induced strain for the model with 10 segments respectively. Suppression of necking is important since the strains inside the cladding tube during the Mandrel test can reach 50 % for ductile cladding tubes. Another interesting feature in Figure 39 is the fact that the location of necking has moved for the 10 segments to the symmetry line and that more extreme necking could be obtained with converged numerical results. The reason for the switch in necking location is not obvious. The most likely reason is that necking occurs at the location with the highest through-wall strain and this changes as the strain concentration gets smaller with 10 segments.

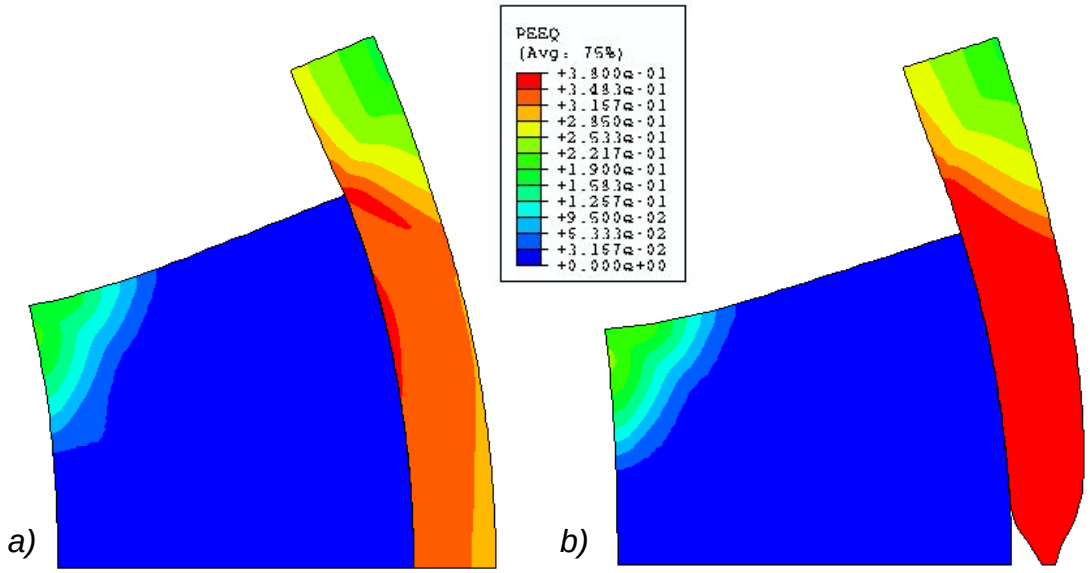

Figure 39: Strain iso-contour plots at maximum computed load for a) 8 segments at Uz = 9 mm (reference), b) 10 segments at Uz =14 mm .

Figure 40 shows the residual strain in the segments after complete unloading from Uz = 9 mm for the 8 and 10 segment models. There are considerable residual strains in the top left corner of the segment, indicating a permanent deformation of the segments after test in both cases but it is smaller for the 10-segment mandrel model.

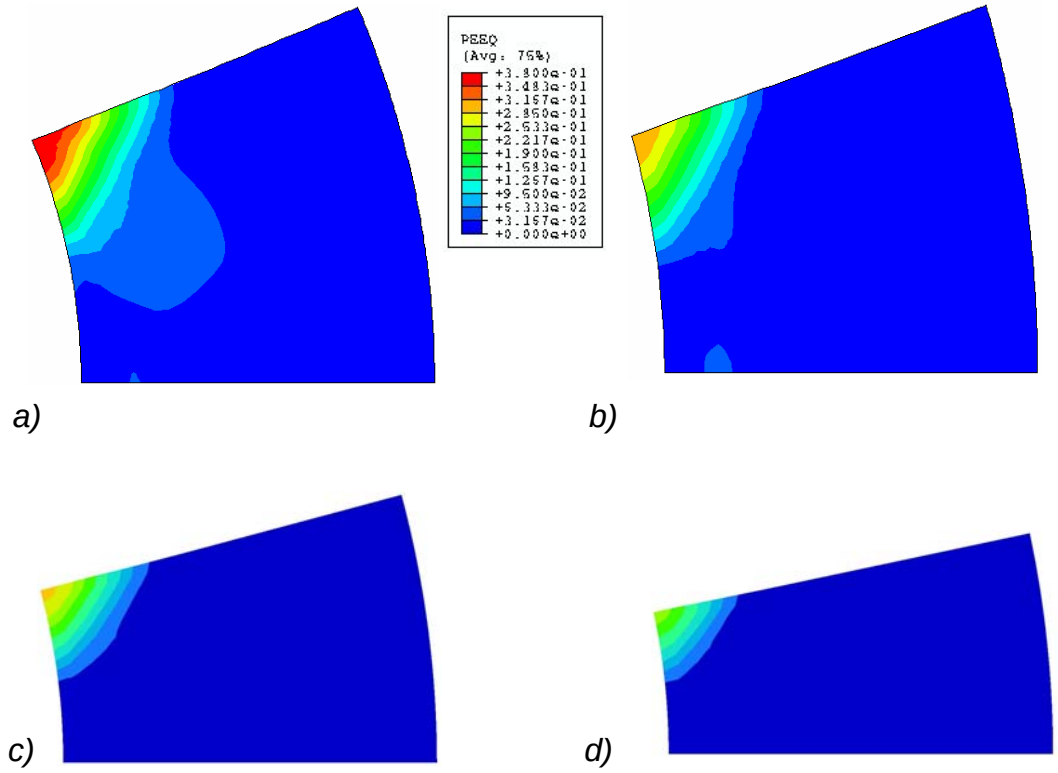

Figure 40: Residual Strains inside segment after loading Uz = 9.6 mm for a) 8 segments (reference), b) 10 segments c) 12 segments, d) 15 segments.

Influence of Friction on the Mandrel Test

From the previous section we have seen that the number of segments has a considerable impact on the strain distribution, weather the strain distribution is more axi-symmetrie. Another parameter which has a large impact on strain distribution is the friction between the segments and the tube. To investigate the influence of friction the analysis for the reference model with 8 segments is repeated with the friction coefficients μ = 0.2, 0.3, 0.4 and 0.5. Figure 41 shows the ratio between largest and smallest hoop strain along the inner edge of the cladding tube vs. the applied displacement for the different friction coefficients. Also here the maximum loads are those for which numerical convergence could be attained for each case. It can be clearly seen that with higher friction coefficients the strain ratio rises considerably. Figure 42 shows the residual strains inside the segments after complete unloading from applied vertical displacement U_z = 9.6 mm for the different friction coefficients. Although the friction coefficient has a large impact on the strain ratio it has a negligible effect on the residual strain.

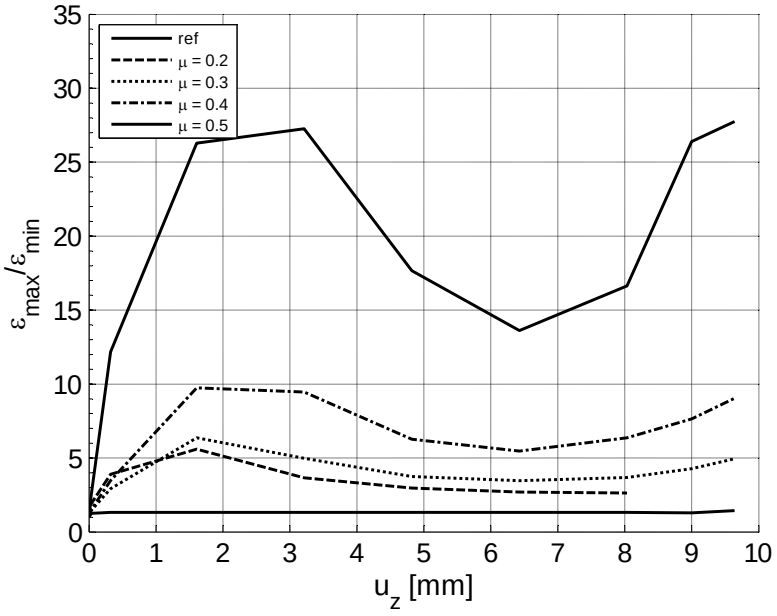

Figure 41: Normalized strain vs. applied displacement for different friction coefficients.

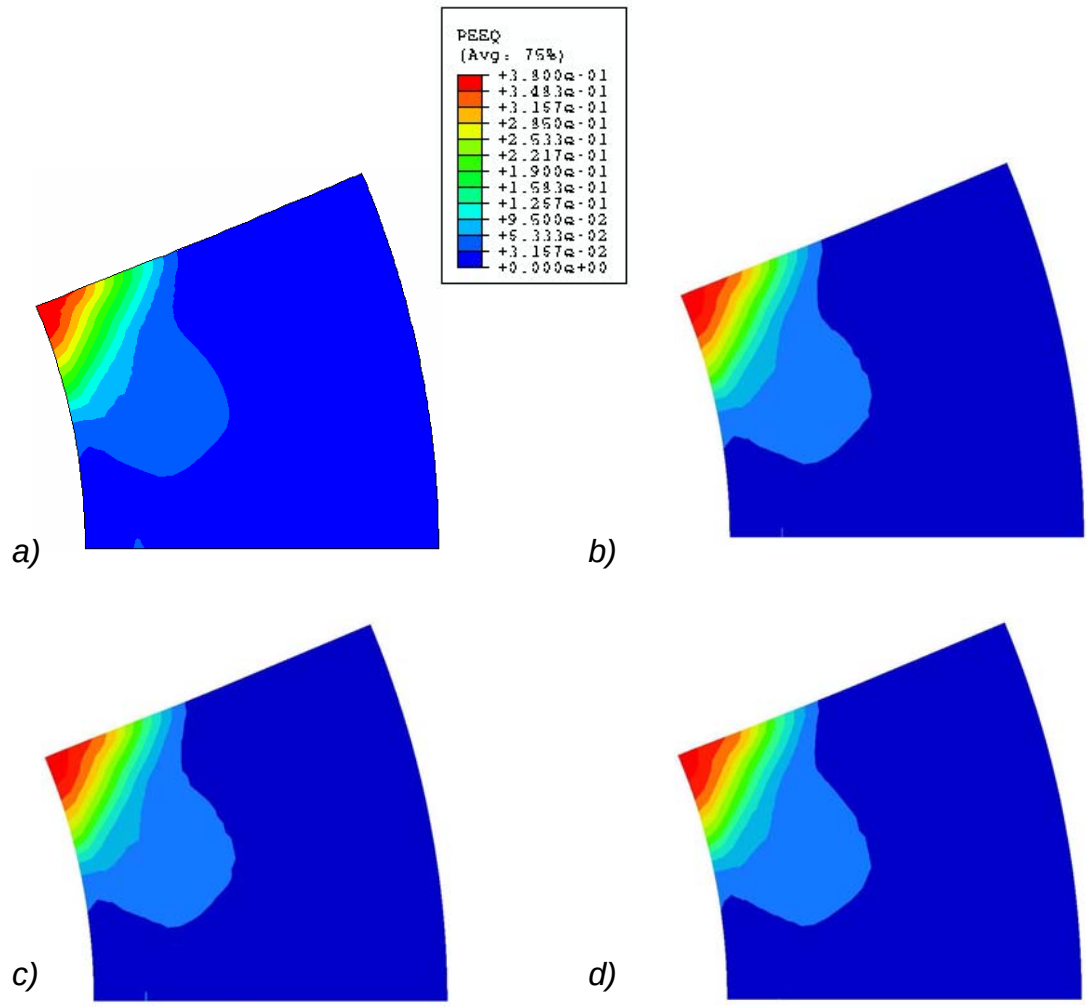

Figure 42: Residual Strains inside segment after loading U_z = 9.6 mm for a) no friction (reference), b) μ=0.3, c) μ=0.4, d) μ=0.5.

Influence of Segment's Material

Another parameter which might have an influence on the strain distribution of the cladding for the Mandrel is the segment's material. To assess the influence of the segment's material the analyses for the reference model are carried out using different stress-strain curves for the segment's material. Figure 43 shows the used stress-strain curves. The upper two curves in Figure 43 are artificial and were created simply by moving up the stress-strain curve for Zircaloy-2.

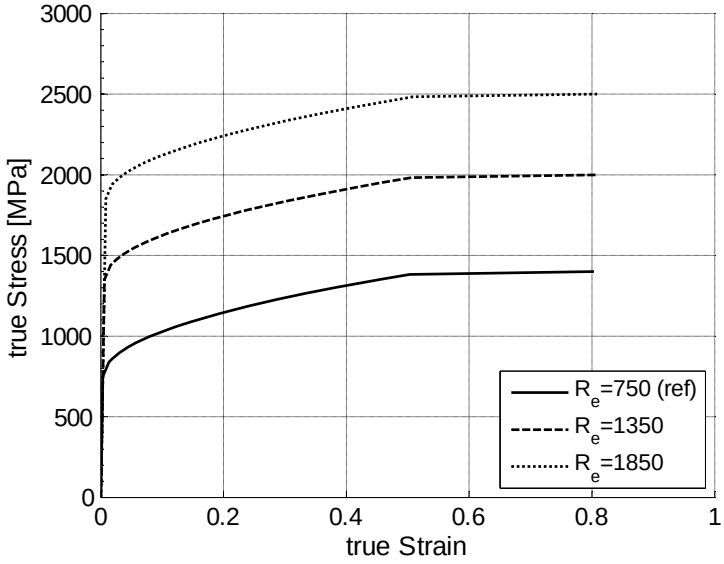

Figure 43: Stress-strain curves used to assess influence of segment's material

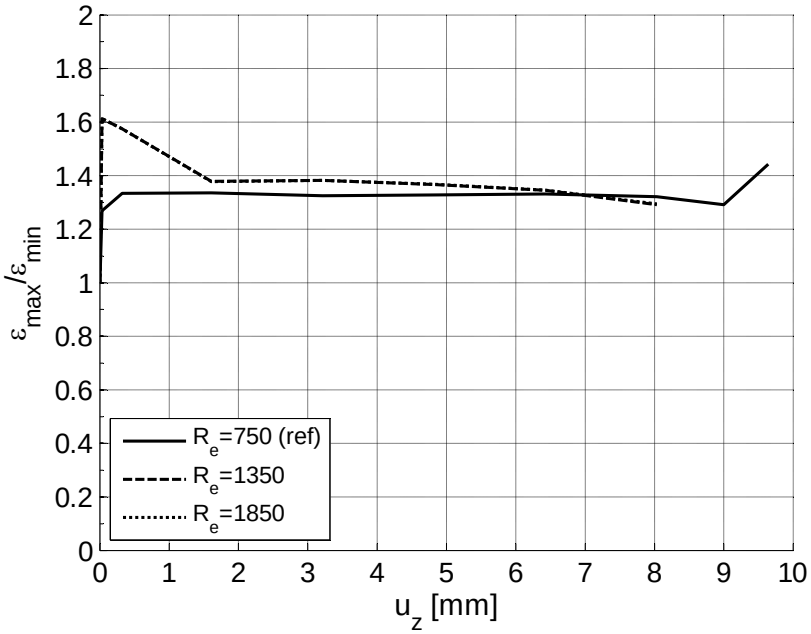

Figure 44 Normalized strain vs. applied displacement for segments with different yield stress.

Figure 44 shows the ratio between largest and smallest hoop strain along the inner edge of the cladding tube vs. the applied displacement for the different stress-strain curves. The curves for the materials with the yield stresses 1350 and 1850 MPa lie above each other and even also compared to the curve for the strain ratio of the regular Zircaloy-2 stress-strain curve there is no significant difference. Thus it can be stated that the segment's material does not have significant impact on the strain distribution inside the cladding within the investigated material property range. Also the effect on the residual strains in the segments after complete unloading is low as Figure 45 shows, which displays the residual strains after loading to U_z = 8.5 mm, which corresponds to 30 % applied strain for the cladding.

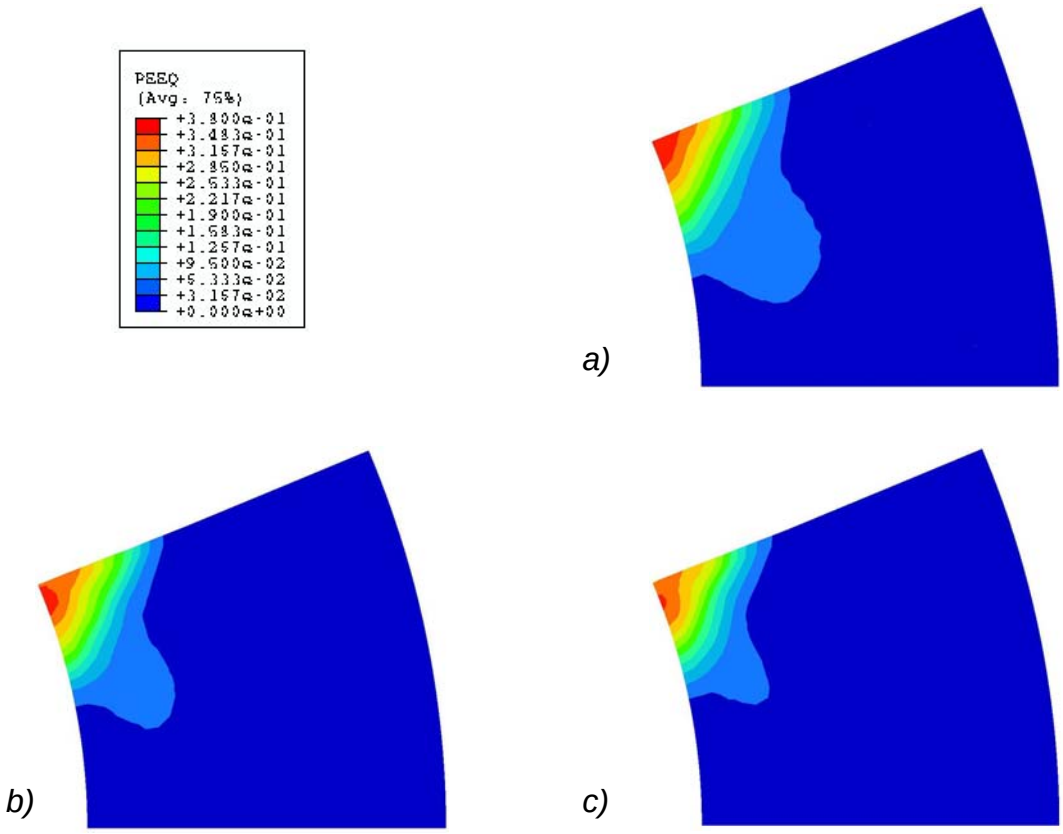

Figure 45: Residual Strains inside segment after loading U_z = 8.5 mm for a) R_e=750 MPa (reference), b) R_e=1350 MPa, c) R_e=1850 MPa.

Conclusions and Recommendations

This report describes the initial development of the Mandrel test for displacement controlled test of nuclear fuel cladding tubes. The following conclusions and recommendations are:

- The trial test show that controlled displacement tests can be performed for a cone-Mandrel with eight segments. The measured hoop strains correspond well with the nominally imposed strains. The gap between the mandrel segments and the tube and variations in distance between segments infer small uncertainty for the actual strains at low loads. The gap can be inferred from the measured strains and imposed displacements and results compensated for this effect. The tests indicated a gap between segment and tube to be about 0.09 mm.
- The tested specimens, which had no hydrides, failed by shear cracking at relatively high loads. Furthermore the test with many unloadings had more hardening indicating a cyclic hardening of the zirconium alloy.
- The finite element computations showed that there is a non-negligible deviation from axi-symmetric loading of the cladding tube. The maximum test load is controlled by the onset of necking. The more axisymmetric the load is, the higher is the load for onset of necking. The segments undergo significant yielding at the inner corners. The deviation from axi-symmetry, load for onset of necking as well as residual deformation of the segments reduces as the number of segments increases. The deviation from axi-symmetry increases with higher friction coefficients between segments and cladding. The effect of friction on the residual strains inside the segments is negligible. The yield and hardening of the segment's material has no significant impact on the axi-symmetry and residual strains inside the segments.

- Based on the tests and supporting FE-analyses we recommend that the number of segments should be at least eight. Too many segments however make the Mandrel impractical for hot-cell testing for which assembly may need to be done remotely. The residual deformation of the segments should be minimized. Friction between segments and cladding should be reduced as much as possible. The optimal design therefore needs to find a compromise between optimal loading situation and practical considerations.

European Commission

EUR 23283 EN– Joint Research Centre – Institute for Energy
Title: Development of the Mandrel Test for Controlled Displacement of Zircaloy Tubes : Summary of Initial Work 2007
Author(s): K-F Nilsson, C. Chanel-Ramos, V. Vokál, J. Mendes and O. Martin
Luxembourg: Office for Official Publications of the European Communities
2008 – 38 pp. – 21 x 29.7 cm
EUR – Scientific and Technical Research series – ISSN 1018-5593

Abstract

This report describes some initial work at IE to develop a displacement controlled test for testing the material properties of spent fuel cladding tubes. The objective is to have a test which allows stable failure under increasing and for which the level of axisymmtery can be controlled. The cone-Mandrel test consists of a set of arc-shaped segments placed inside a section of a Zircaloy tube and pushed outwards by the vertical displacement of a conical shaft. The cone-mandrel is first developed for un-irradiated conditions but the test should also be applicable for irradiated components in hot cells at ITU. The report describes the practical implementation of the cone-mandrel with 8 segments and applied to three specimens. The tests show that the cone-mandrel can be used to attain controlled displacements until failure. The load is not accurately monitored for very low loads due to misalignment between cone, segments and tube. It is, however, straight-forward to compensate for this effect from the registered displacement/strain curve. The tested specimens were subsequently analysed by fractographic studies. The main fracture was by shearing along lines that make 45° angle with the axial and circumferential directions. The tests were simulated by non-linear finite element (FE) calculations. The finite element calculations simulated the experimental observations quite well. The FE calculations also allowed us to better understand the failure by necking and the deviation of axi-symmetric loading due to stress concentrations at the end of the segments. Furthermore the cone is also subjected to plastic deformation. The plastic deformation of the cone and the deviation from axi-symmetric load conditions can be reduced by increasing the number of segments. To this end mandrels with 6, 8 and 10 segments were analysed. The conclusion is that one should use at least 8 segments and that one should use a harder material for the cone.

How to obtain EU publications

Our priced publications are available from EU Bookshop (http://bookshop.europa.eu), where you can place an order with the sales agent of your choice.

The Publications Office has a worldwide network of sales agents. You can obtain their contact details by sending a fax to (352) 29 29-42758.

The mission of the JRC is to provide customer-driven scientific and technical support for the conception, development, implementation and monitoring of EU policies. As a service of the European Commission, the JRC functions as a reference centre of science and technology for the Union. Close to the policy-making process, it serves the common interest of the Member States, while being independent of special interests, whether private or national.